



Enhanced gas-phase photocatalytic removal of aromatics over direct Z-scheme-dictated $H_3PW_{12}O_{40}/g\text{-}C_3N_4$ film-coated optical fibers

Jiaqi Meng, Xinyue Wang, Xia Yang, An Hu, Yihang Guo*, Yuxin Yang*

School of Environment, Northeast Normal University, Changchun 130117, PR China



ARTICLE INFO

Keywords:

Volatile organic compound
Photocatalysis
Z-scheme
Graphitic carbon nitride
Polyoxometalate

ABSTRACT

Environmentally benign photocatalytic oxidation is one of the most promising approaches to remove volatile, highly toxic and refractory aromatics, and the key points of gas-phase photocatalytic oxidation of aromatics are to develop efficient photocatalysts and design suitable photoreactors. Here, the custom-designed $H_3PW_{12}O_{40}/g\text{-}C_3N_4$ film-coated optical fiber photoreactor is demonstrated for gas-phase simulated sunlight photocatalytic removal of aromatics including benzene, toluene and *m*-xylene. At relative humidity of 73% and air atmosphere, the $H_3PW_{12}O_{40}/g\text{-}C_3N_4$ film-coated optical fibers with $H_3PW_{12}O_{40}$ doping level of 3.2% exhibit remarkably higher photocatalytic removal efficiency of benzene, toluene and *m*-xylene than that of the $g\text{-}C_3N_4$ film, and apparent rate constant of the $H_3PW_{12}O_{40}/g\text{-}C_3N_4$ film for benzene, toluene and *m*-xylene removal is 2.42, 1.75 and 3.67 times higher than that of $g\text{-}C_3N_4$ film. The enhanced photocatalytic activity of the $H_3PW_{12}O_{40}/g\text{-}C_3N_4$ film is ascribed to direct Z-scheme-dictated charge carrier migration mechanism, imparting not only superior photogenerated charge carrier separation ability but also undiminished redox capability of the photogenerated electrons and holes; additionally, the increased contact area of catalyst film with the substrates and improved light harvesting ability give rise to the important contribution to gas-phase photocatalytic removal of aromatics. Moreover, the catalyst film exhibits excellent adhesion, stability and recyclability, and the activity loss is negligible after total thirty times' catalytic runs.

1. Introduction

Inevitable presence of hazardous volatile organic compound (VOC) emission in indoor and outdoor environment is the result of rapid urbanization and industrialization accompanying with the increase of fossil fuel consumption for transportation, and the caused indoor and outdoor air pollution represents a severe challenging public health issue that has been receiving increasing attention worldwide [1–3]. VOCs mainly contain alkanes, aromatics, esters, alkenes, carboxylic acids and alcohols [4], in which highly toxic and refractory BTEX (Benzene, Toluene, Ethylbenzene and Xylenes) are among the top priority VOC effluents [5]. In the search for advanced VOC removal technologies to remediate air pollution and improve air quality, environmentally benign photocatalytic oxidation (PCO) is regarded as one of the most promising approaches, and it has become the focus of the relevant research works [1]. TiO_2 -based PCO of VOC is extensively studied [6–11], nevertheless, TiO_2 photocatalyst suffers from shortcoming of poor solar energy utilization, which greatly limits its practical applications in VOC removal. Accordingly, the key point of sustainable photocatalytic VOC oxidation technology is to develop sunlight/visible-light driven

photocatalysts; in addition, rational design of highly efficient photo-reactors for VOC removal is also the utmost important.

Bearing both issues in mind, in the present work, we demonstrate a direct Z-scheme-dictated $H_3PW_{12}O_{40}/g\text{-}C_3N_4$ film-coated optical fiber photoreactor for efficient removal of aromatics including benzene, toluene and *m*-xylene in the gas-phase under simulated sunlight irradiation. Metal-free and sustainable graphitic carbon nitride ($g\text{-}C_3N_4$) with suitable band gap is the promising candidate of new generation sunlight/visible-light-responsive photocatalyst [12–14]. However, bulk $g\text{-}C_3N_4$ suffers from a low efficiency in photocatalytic applications because of high recombination probability of the photogenerated charge carriers (e_{CB}^- and h_{VB}^+) and small BET surface area (lower than $10\text{ m}^2\text{ g}^{-1}$ for bulk $g\text{-}C_3N_4$ [15]). Construction of heterojunctions between $g\text{-}C_3N_4$ and other semiconductors is one of the effective approaches to improve the photocatalytic activity of $g\text{-}C_3N_4$ via delay the recombination of e_{CB}^- and h_{VB}^+ [16–20]. Particularly, great interest has been paid in the design of $g\text{-}C_3N_4$ -based Z-scheme-dictated heterojunctions such as $g\text{-}C_3N_4/TiO_2$, $g\text{-}C_3N_4/Ag_2WO_4$, $CDs/g\text{-}C_3N_4/MoO_3$, $WO_3/g\text{-}C_3N_4$ and $Sn_3O_4/g\text{-}C_3N_4$ [21–25]. Polymeric $g\text{-}C_3N_4$ is one the most suitable candidates for the fabrication of direct Z-scheme-

* Corresponding authors.

E-mail addresses: guoyh@nenu.edu.cn (Y. Guo), yangyx374@nenu.edu.cn (Y. Yang).

dictated photocatalysts because it has less positive valence band (VB) edge potential and more negative conduction band (CB) edge potential [26]. Remarkably enhanced photocatalytic activity of $g\text{-C}_3\text{N}_4$ -based Z-scheme heterojunctions is due to unique photogenerated charge carrier migration mode, leading to superior photogenerated charge carrier separation ability and undiminished redox capability of e_{CB}^- and h_{VB}^+ [25,27–32].

Polyoxometalates (POMs) are a large and promptly growing class of transition metal-oxygen clusters with significant applications in catalysis, thanks to their unique chemical structure and thereby reversible redox properties [33–36]. POMs share very similar photochemical characteristics to the semiconductors including well-defined HOMO-LUMO gap, and the photocatalytic performance of POMs is originated from the photoexcitation of the oxygen-to-metal charge transfer to yield e_{CB}^- and h_{VB}^+ . The Keggin structured $\text{H}_3\text{PW}_{12}\text{O}_{40}$ is one of the most explored POMs in photocatalysis, however, it suffers from the drawbacks of limited solar light utilization efficiency and fast recombination probability of e_{CB}^- and h_{VB}^+ . Fabrication of direct Z-scheme-dictated $\text{H}_3\text{PW}_{12}\text{O}_{40}/g\text{-C}_3\text{N}_4$ heterojunctions is feasible because of well-matched energy band structures of $\text{H}_3\text{PW}_{12}\text{O}_{40}$ (more positive HOMO level and less negative LUMO level [37]) and $g\text{-C}_3\text{N}_4$ (less positive VB edge potential and more negative CB edge potential), which is favorable for the migration of e_{CB}^- on the LUMO of $\text{H}_3\text{PW}_{12}\text{O}_{40}$ directly to the VB of $g\text{-C}_3\text{N}_4$ and then further recombination with h_{VB}^+ of $g\text{-C}_3\text{N}_4$. This unique photogenerated charge carrier separation and migration pathway gives rise to the generation of plentiful active oxygen species like superoxide radical (O_2^-) and hydroxyl radical (OH^\cdot) to participate in the oxidation of gaseous aromatics, which compensates the moderate oxidation ability of pure $g\text{-C}_3\text{N}_4$, causing to deep oxidation of the target pollutants.

The other challenge is to design highly efficient photoreactors for gas-phase removal of VOCs. Unlike conventionally used photoreactors for liquid-phase PCO reactions based on the slurry system with suspended photocatalysts, gas-phase treatment systems usually employ the immobilized photocatalysts. The wall of the reactor [38], support substrates [39], metallic materials [40], molecular sieve [41] and activated carbon fiber [42] are generally applied for immobilization of the catalysts in gas-phase PCO of VOCs. The main obstacle of VOC removal in the aforementioned systems is considerably low efficiency because of the limited coating area and low light harvesting ability of the photocatalysts. Aiming at to improve the PCO removal efficiency of VOCs, here, a custom-designed optical fiber photoreactor that incorporates a number of parallel optical fiber bundles for both light transmission and the support of the $\text{H}_3\text{PW}_{12}\text{O}_{40}/g\text{-C}_3\text{N}_4$ catalyst is presented. The coating area of the $\text{H}_3\text{PW}_{12}\text{O}_{40}/g\text{-C}_3\text{N}_4$ film is significantly increased; meanwhile, light utilization efficiency is enhanced owing to unique light transmission mode of optical fibers [43–46]. For the design and preparation of the $\text{H}_3\text{PW}_{12}\text{O}_{40}/g\text{-C}_3\text{N}_4$ film coated optical fibers, special attentions are paid on: (i) design of suitable $\text{H}_3\text{PW}_{12}\text{O}_{40}/g\text{-C}_3\text{N}_4$ film coating technique to ensure enough stability or adhesion of the film on the optical fibers, and thereby the drop of the film from the support is prevented; and (ii) the drop of the Keggin units from the $\text{H}_3\text{PW}_{12}\text{O}_{40}/g\text{-C}_3\text{N}_4$ film during preparation and subsequent aqueous solution washing process should be controlled because $\text{H}_3\text{PW}_{12}\text{O}_{40}$ shows high solubility in water.

In the custom-designed $\text{H}_3\text{PW}_{12}\text{O}_{40}/g\text{-C}_3\text{N}_4$ film-coated optical fiber photoreactor, simulated sunlight photocatalytic removal of benzene, toluene and *m*-xylene in the gas-phase is evaluated, and the influence of the important experimental parameters including relative humidity (RH) and the concentration of oxygen on the pollutant removal efficiency is studied. The enhanced photocatalytic activity of the $\text{H}_3\text{PW}_{12}\text{O}_{40}/g\text{-C}_3\text{N}_4$ film as compared with pure $g\text{-C}_3\text{N}_4$ film is mainly explained by the direct Z-scheme-dictated charge carrier separation and migration mechanism, which is directly evidenced by the generation of plentiful O_2^- and OH^\cdot radicals in the systems; meanwhile, the $\text{H}_3\text{PW}_{12}\text{O}_{40}/g\text{-C}_3\text{N}_4$ film also shows stronger ability in photoreduction

of Cr(VI) to Cr(III), providing indirect evidence to further confirm the Z-scheme configuration of the $\text{H}_3\text{PW}_{12}\text{O}_{40}/g\text{-C}_3\text{N}_4$. More importantly, owing to carefully designed preparation technique of the $\text{H}_3\text{PW}_{12}\text{O}_{40}/g\text{-C}_3\text{N}_4$ film-coated optical fibers, the catalyst film can be reused at least for total thirty times without obvious activity loss, and the drop of the Keggin units from the catalyst film is hardly occurred, exhibiting potential of practical applications in removal of VOCs effectively and conveniently.

2. Experimental

2.1. Preparation of the $\text{H}_3\text{PW}_{12}\text{O}_{40}/g\text{-C}_3\text{N}_4$ film-coated optical fiber bundles

2.1.1. Ultrathin $g\text{-C}_3\text{N}_4$ nanosheets

Bulk $g\text{-C}_3\text{N}_4$ powder was firstly prepared by heating urea (50 g) in a muffle furnace under the temperature programming of 250 °C for 1 h, 350 °C for 2 h and a final temperature 550 °C for 2 h with a rate of 2 °C min^{-1} . The formed yellow powder was cooled and then washing with HNO_3 (0.1 mol L^{-1}) and distilled water, respectively. The bulk $g\text{-C}_3\text{N}_4$ powder thus obtained (1.5 g) was dispersed to an aqueous HCl solution (14.8%, 250 mL). The resulting suspension was sonicated for 1 h followed by magnetically stirring for 24 h, and then it was hydrothermally treated at 110 °C for 5 h. The cooled precipitate was pump filtrated and then washed with water completely until the effluent became neutral, after drying at 80 °C ultrathin $g\text{-C}_3\text{N}_4$ nanosheets that were proved to more photocatalytic active than urea-derived bulk $g\text{-C}_3\text{N}_4$ [47] were obtained.

2.1.2. $\text{H}_3\text{PW}_{12}\text{O}_{40}/g\text{-C}_3\text{N}_4$ film-coated optical fiber bundles

At first, $\text{H}_3\text{PW}_{12}\text{O}_{40}/\text{SiO}_2$ sol was prepared for subsequent fabrication of $\text{H}_3\text{PW}_{12}\text{O}_{40}/g\text{-C}_3\text{N}_4$ film. Typically, tetraethyl orthosilicate (TEOS, 5 mL) was dissolved in ethanol (2.6 mL) under vigorous stirring for 30 min, and then $\text{H}_3\text{PW}_{12}\text{O}_{40}$ (0.34 or 0.68 mmol to adjust acidity of the system and $\text{H}_3\text{PW}_{12}\text{O}_{40}$ loading level simultaneously) was added. The mixture was refluxed at 78 °C for 40 min to obtain $\text{H}_3\text{PW}_{12}\text{O}_{40}/\text{SiO}_2$ sol with suitable viscosity.

Next, $\text{H}_3\text{PW}_{12}\text{O}_{40}/g\text{-C}_3\text{N}_4$ (SiO_2) suspension with suitable viscosity was prepared following the procedure described below. Ultrathin $g\text{-C}_3\text{N}_4$ nanosheets (2.5 g) was completely dispersed into the mixture of ethanol (30 mL) and freshly prepared $\text{H}_3\text{PW}_{12}\text{O}_{40}/\text{SiO}_2$ sol (1 mL), and the resulting mixture was stirred for 1 h to the desired suspension.

Finally, the $\text{H}_3\text{PW}_{12}\text{O}_{40}/g\text{-C}_3\text{N}_4$ (SiO_2) film-coated optical fiber bundles were prepared by dip-withdrawing method. Each optical fiber (length 80 mm and diameter 0.6 mm) used here was composed of double layers with a polymer cladding surrounded by the quartz core. Before coating, the polymer cladding was removed by calcination at 450 °C for 3 h, and the nude optical fibers were washed by NaOH solution (5 mol L^{-1}) for 30 min in an ultrasonic bath to remove organic contaminants and fine particles on the surface. Subsequently, the nude optical fibers were washed thoroughly with distilled water and then dried at 80 °C. The fresh nude quartz fiber bundles were dipped into the newly prepared $\text{H}_3\text{PW}_{12}\text{O}_{40}/g\text{-C}_3\text{N}_4$ (SiO_2) suspension and kept for 3 min, and then the $\text{H}_3\text{PW}_{12}\text{O}_{40}/g\text{-C}_3\text{N}_4$ (SiO_2) film-coated optical fiber bundles were withdrawn from the suspension. After drying at room temperature, the dip-withdrawing procedure was repeated for 6 times to obtain the film with appropriate thickness. After drying at room temperature for 12 h, the $\text{H}_3\text{PW}_{12}\text{O}_{40}/g\text{-C}_3\text{N}_4$ (SiO_2) film-coated quartz fiber bundles were heated at 40 °C for 2 h, 60 °C and 80 °C for 1 h, successively. Finally, the coated optical fibers were washed with distilled water to remove the loosely attached catalyst particles on the surface. After being dried at 80 °C, the $\text{H}_3\text{PW}_{12}\text{O}_{40}/g\text{-C}_3\text{N}_4$ (SiO_2) film-coated quartz fiber bundles were obtained, and they are abbreviated as $\text{PW}_{12}/g\text{-C}_3\text{N}_4\text{-}x$ film with “ x ” representing $\text{H}_3\text{PW}_{12}\text{O}_{40}$ loading level in the coated film. Here “ x ” was determined by a Leeman Prodigy Spec (I) ICP-AES, and it equaled to 1.1 and 3.2 wt%, respectively.

For comparison, HCl-derived SiO_2 sol was also prepared by hydrolysis of TEOS at 78 °C for 40 min, and then $\text{g-C}_3\text{N}_4$ (SiO_2) suspension with suitable viscosity was obtained following the same procedure for the preparation of the $\text{H}_3\text{PW}_{12}\text{O}_{40}/\text{g-C}_3\text{N}_4$ (SiO_2) suspension. Afterwards, $\text{g-C}_3\text{N}_4$ film-coated optical fiber bundles were prepared via the same method with the $\text{PW}_{12}/\text{g-C}_3\text{N}_4$ film-coated optical fiber bundles.

2.2. Characterization of the $\text{H}_3\text{PW}_{12}\text{O}_{40}/\text{g-C}_3\text{N}_4$ film or powder

XRD measurement was performed on a Japan Rigaku D/max 2000 X-ray diffractometer. TEM observation was carried out on a JEM-2100 high resolution transmission electron microscope at an accelerating voltage of 200 kV. FESEM observation was performed on a XL-30 ESEMFESEM field emission scanning electron microscope. FT-IR spectra were recorded on a Nicolet Magna 560 IR spectrophotometer. XPS was recorded on a VG-ADES 400 instrument with Mg Ka-ADES source at a residual gas pressure of lower than 10^{-8} Pa. ^{31}P MAS NMR and ^{13}C CP-MAS NMR spectra were recorded on a Bruker AVANCE III 400 WB spectrometer equipped with a 4 mm standard bore CP MAS probe head. Nitrogen gas porosimetry measurement was performed on a Micrometrics ASAP 2020 M PLUS HD88 surface area and porosity analyzer. UV-vis/DRS was recorded on a Cary 500 UV-vis-NIR spectrometer. Electron spin resonance (ESR) spectra were recorded on a JES-FA200 ESR spectrometer (central field 337 mT, power 1 mW, modulation amplitude 8000). 5,5-dimethyl-1-pyrroline-N-oxide (DMPO) was employed as a spin trap in the detection of radicals, and it was stored at -20 °C and in the dark until required. Distilled water and methanol employed for ESR measurement were gently bubbled with nitrogen gas for 20 min. After the catalyst (2 mg) was dispersed in treated distilled water (2.0 mL) for the $^{\cdot}\text{OH}$ adduct and treated methanol (2.0 mL) for $^{\cdot}\text{O}_2^-$ adduct measurements, DMPO (28 μL) was added.

2.3. Photocatalytic removal of gaseous aromatics over the $\text{H}_3\text{PW}_{12}\text{O}_{40}/\text{g-C}_3\text{N}_4$ film-coated optical fibers

Gas-phase photocatalytic removal of aromatics including benzene, toluene and *m*-xylene was performed in a custom-designed quartz reactor (300 mL) that was gas-tight and equipped with a removable cover. In this reactor, the catalyst film-coated quartz fiber bundles (composed of 278 pieces of the coated quartz fibers with the catalyst mass of 135 mg) were fixed on the channels of perforated Teflon plate, and the plate was placed vertically throughout the reactor. The external simulated sunlight irradiation was supplied by a PLS-SXE300 Xe lamp (300 W) with IR and 320 nm cut filters.

The vapors of the pollutants were generated by evaporation of liquid benzene, toluene and *m*-xylene in the photoreactor, respectively. Typically, 2 μL of benzene, toluene or *m*-xylene was injected into the reactor, and then the reactor was sealed by sealing clips. The reactor was put into the oven and heated to 40 °C (for benzene), 45 °C (for toluene and *m*-xylene) to ensure the complete evaporation of liquid aromatic pollutants; meanwhile, the adsorption-desorption equilibrium between the $\text{PW}_{12}/\text{g-C}_3\text{N}_4$ film and pollutant molecules reached. After the above process, 500 μL of the evaporated reactant gases were taken out and then fully dissolved in 1 mL of acetonitrile. The initial concentration (c_0) of each pollutant in the closed loop reactor was determined by an Agilent 1200 HPLC: C18 column; UV detector ($\lambda = 204$, 215 and 215 nm, respectively); methanol/water (90/10, v/v); 1.0 mL min^{-1} . The photocatalytic removal of gaseous aromatics was carried out at ambient temperature, RH of 73% (adjusted by the introduction of water vapor) and air atmosphere. Changes of the concentrations (c_t) of each pollutant during the photocatalytic process were also monitored by HPLC after the withdrawn gaseous samples (500 μL) were fully dissolved in acetonitrile (1 mL). Organic acids produced during the process of photocatalytic removal of aromatics were

determined qualitatively and quantitatively by a Dionex DX-300 ion chromatography (IC) equipped with an ICE-AS6 analytical column and CDM-II conductivity detector. The other intermediates generated during the above photocatalytic process were identified by an Agilent 1200 HPLC/MicrOTOFESI-TOF-MS high-resolution electrospray ionization time-of-flight mass spectrometry equipped with high performance liquid chromatography (HPLC-MS).

The photocatalytic reduction of Cr(VI) to Cr(III) over the $\text{PW}_{12}/\text{g-C}_3\text{N}_4$ (SiO_2)-3.2 powder was evaluated in a self-made quartz reactor that was fitted with a circulation water system to maintain a constant reaction temperature (25 °C). Typically, $\text{PW}_{12}/\text{g-C}_3\text{N}_4$ (SiO_2)-3.2 powder (100 mg) was dispersed in an aqueous $\text{K}_2\text{Cr}_2\text{O}_7$ solution (100 mL) with initial concentration of Cr(VI) of 20 mg L^{-1} and pH = 2.68. The suspension obtained was ultrasonicated for 10 min and stirred in the dark to accomplish adsorption-desorption equilibrium. Subsequently, the suspension was irradiated under the simulated sunlight for 120 min. Changes of the concentrations of Cr(VI) were determined by diphenylcarbazide method using a Cary 60 UV-vis-NIR spectrometer at $\lambda = 540$ nm [48].

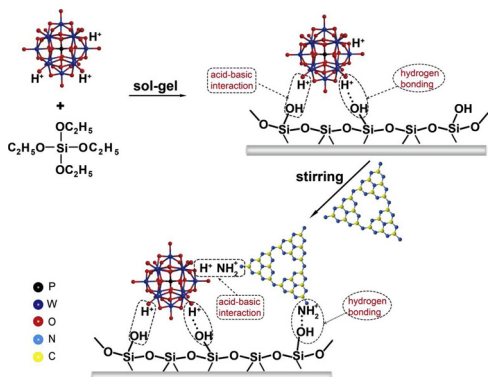
2.4. Photoelectrochemical measurements

All electrochemical measurements were carried out in a conventional three-electrode electrochemical workstation system (CHI 660E, China) equipped with an Ag/AgCl (saturated KCl), a Pt wire and an L-type glassy carbon electrode covered with the catalyst film on the black round area (diameter of 3.0 mm and area of 7.06 mm^2) served as the reference electrode, counter electrode and working electrode, respectively (Fig. S1 of supplementary information). The simulated sunlight provided by the Xe lamp irradiated the glassy carbon electrode from the side. The transient photocurrent measurement was carried out in a 0.01 mol L^{-1} Na_2SO_4 solution and recorded by i - t curves with a bias voltage of +1.0 V for 200 s, the Mott-Schottky measurement of $\text{g-C}_3\text{N}_4$ nanosheets was performed in a 0.5 mol L^{-1} Na_2SO_4 solution and recorded by $1/C^2$ - V plot, and the cyclic voltammogram plot of the starting $\text{H}_3\text{PW}_{12}\text{O}_{40}$ was measured in a 0.1 mol L^{-1} $\text{Na}_2\text{SO}_4/\text{H}_2\text{SO}_4$ aqueous solution (pH = 1.5, and the concentration of $\text{H}_3\text{PW}_{12}\text{O}_{40}$ was 1×10^{-3} mol L^{-1}) and recorded by i - V curves.

3. Results and discussion

3.1. Preparation and characterization of the $\text{PW}_{12}/\text{g-C}_3\text{N}_4$ film-coated optical fibers

For the preparation of stable and recoverable $\text{PW}_{12}/\text{g-C}_3\text{N}_4$ film-coated optical fibers, the $\text{PW}_{12}/\text{g-C}_3\text{N}_4$ suspension must have suitable viscosity to ensure the films adhering on the optical fibers firmly. Here, freshly prepared $\text{PW}_{12}/\text{SiO}_2$ sol is successfully applied to the preparation of $\text{PW}_{12}/\text{g-C}_3\text{N}_4$ suspension with enough viscosity; meanwhile, as-designed sol-gel method can immobilize the Keggin units on the silica framework via acid-base and hydrogen bonding interactions. As illustrated in Scheme 1, during the process of hydrolysis and condensation of TEOS in the presence of $\text{H}_3\text{PW}_{12}\text{O}_{40}$, chemically active surface silanol groups ($\equiv\text{Si}-\text{OH}$) from the formed silica framework are protonated by $\text{H}_3\text{PW}_{12}\text{O}_{40}$ to form $\equiv\text{Si}-\text{OH}_2^+$ groups, and the $\equiv\text{Si}-\text{OH}_2^+$ groups act as the counter ions for the $\text{H}_2\text{PW}_{12}\text{O}_{40}^-$ to yield $[\equiv\text{Si}-\text{OH}_2^+] [\text{H}_2\text{PW}_{12}\text{O}_{40}^-]$ species through acid-base reaction [35,49]; additionally, protons from the Keggin units may also interact with $\equiv\text{Si}-\text{OH}$ groups through hydrogen bonding. In the following preparation of the $\text{PW}_{12}/\text{g-C}_3\text{N}_4$ suspension, the $-\text{NH}_2$ groups from the edges of $\text{g-C}_3\text{N}_4$ polymer [50] are protonated by $\text{H}_3\text{PW}_{12}\text{O}_{40}$ to form $[-\text{NH}_3^+] [\text{H}_2\text{PW}_{12}\text{O}_{40}^-]$ species at the interface of both components. This acid-base interaction renders the Keggin units bonding to the $\text{g-C}_3\text{N}_4$ polymer strongly. Consequently, leakage of the Keggin unit from the catalyst film is expected to be avoided effectively; meanwhile, the strong interactions between the Keggin unit and $\text{g-C}_3\text{N}_4$ polymer is



Scheme 1. Schematic illustration of the route for the preparation of PW₁₂/g-C₃N₄ films and their framework structure.

expected to facilitate the separation and migration of the photo-generated charge carriers. Additionally, the $-\text{NH}_2$ groups from the edges of g-C₃N₄ polymer may also interact with $\equiv\text{Si}-\text{OH}$ groups of silica framework through hydrogen bonding.

3.1.1. Composition and structural information

XRD patterns shown in Fig. 1a indicate that four tested g-C₃N₄-based samples all exhibit two characteristic diffraction peaks at 20 values of 13.1 and 27.4°. The first peak represents in-plane structural packing motif with a period of 0.675 nm and is indexed as the (100) crystal plane of g-C₃N₄, while the second peak corresponding to the interlayer stacking of aromatic units of CN with an interlayer distance of 0.33 nm is ascribed to the (002) plane of the stacking of the conjugated aromatic system [51,52]. The result implies that the basic atomic crystal structure of g-C₃N₄ remains intact after the formation of the PW₁₂/g-C₃N₄ films. Additionally, any diffraction peak originated from the Keggin units is hardly found, suggesting homogeneous dispersion of the Keggin units throughout the ultrathin g-C₃N₄ nanosheets.

FT-IR spectra can further provide the structure information

concerning about g-C₃N₄ and the Keggin unit in the PW₁₂/g-C₃N₄ films (Fig. 1b). For the starting g-C₃N₄ powder or film, the sharp peak at 810 cm⁻¹ is assigned to the breathing mode of tri-s-triazine units [53], several weak peaks in the range of 1636 to 1206 cm⁻¹ are originated from the stretching vibrations of C=N and C≡N bonds in the CN heterocycles [46], and the broad absorption peaks located at 3300 to 3000 cm⁻¹ are due to the stretching vibration of N–H and O–H bonds [54,55]. In addition, compared with g-C₃N₄ powder, a new and small peak is detected at 1086 cm⁻¹ for g-C₃N₄ film, which is assigned to the vibration of Si–O–Si bonds of the included silica. The starting H₃PW₁₂O₄₀ has four characteristic vibrational peaks positioned at 1082, 986, 885 and 809 cm⁻¹, attributing to vibrations of P–O_a bonds of the PO₄ tetrahedron, terminal W=O_d bonds and two bridge W–O_b/c–W bonds, respectively [56]. The characteristic vibrational peaks related to the starting g-C₃N₄ and Keggin unit can also be found in the PW₁₂/g-C₃N₄-1.1 film and PW₁₂/g-C₃N₄-3.2 film, suggesting the structural integrity of both components after sol-gel process and subsequent treatment. Since some characteristic vibrational peaks of g-C₃N₄ and silica also appear in the range from 800 to 1100 cm⁻¹, the powerful evidence to confirm the retention of both graphite-like and Keggin structures in the PW₁₂/g-C₃N₄ film is provided by ¹³C CP-MAS NMR and ³¹P MAS NMR spectra. As displayed in Fig. 1c, the peaks at 156.0 and 164.3 ppm are assigned to the carbon atoms from CN₃ (C¹) and CN₂(NH)₂ (C²) moieties, respectively, in g-C₃N₄ [57,58]. From the result shown in Fig. 1d it is found that the PW₁₂/g-C₃N₄-3.2 film exhibits a strong resonance signal at -17.5 ppm, characteristics of the symmetric central P atom from PO₄ tetrahedron of the Keggin unit; additionally, slight down-field shift as compared with the parent H₃PW₁₂O₄₀ (-16.5 ppm) [59] originates from the acid-base interactions between the H₃PW₁₂O₄₀ and g-C₃N₄, which causes somewhat perturbation of the chemical environment of the Keggin units at the interface of both components.

High-resolution XPS data collected for the starting g-C₃N₄ powder and PW₁₂/g-C₃N₄-3.2 film also verify their graphite-like structure; meanwhile, the data reflect the interactions between g-C₃N₄ and Keggin units in as-prepared film. Deconvoluted C 1s spectrum of the starting g-

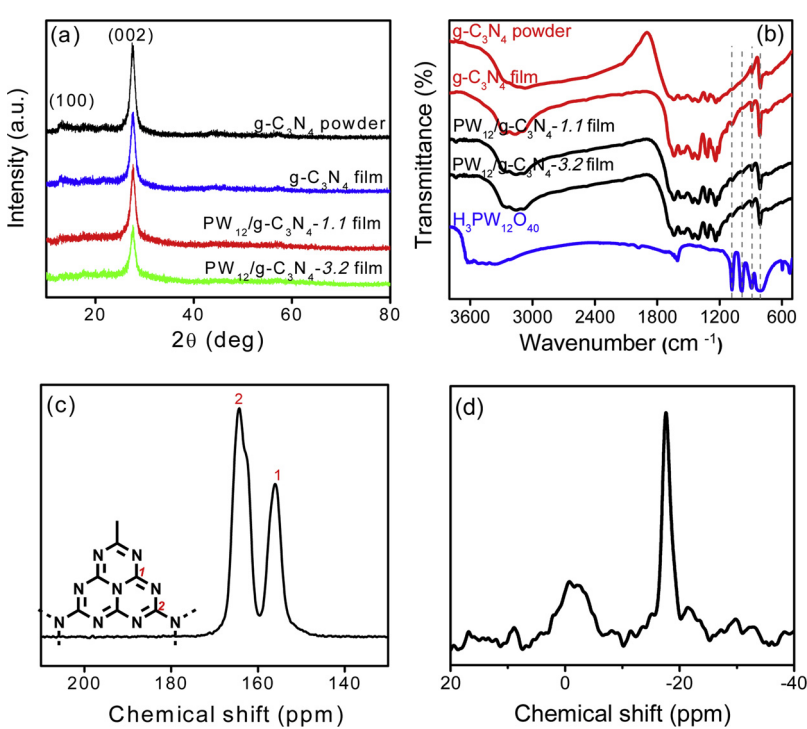


Fig. 1. XRD patterns (a), FT-IR spectra (b) of g-C₃N₄ and PW₁₂/g-C₃N₄ powder/films. ¹³C CP-MAS NMR (c) and ³¹P MAS NMR spectra (d) of the PW₁₂/g-C₃N₄-3.2 film.

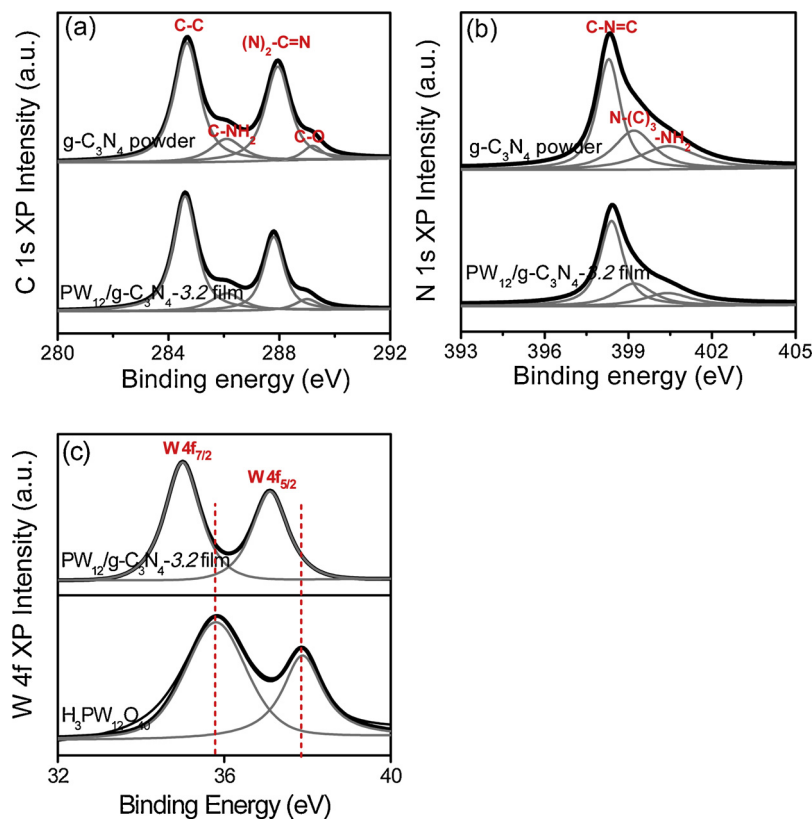


Fig. 2. High-resolution XPS spectra of g-C₃N₄ powder and PW₁₂/g-C₃N₄-3.2 film in the C 1s (a), N 1s (b) and W 4f (c) binding energy regions.

C₃N₄ shows two main signals centered at 284.6 and 288.0 eV (Fig. 2a), corresponding to graphitic carbon species and sp²-bonded carbon in C=N coordination, respectively [60,61]; additionally, the other two weak peaks positioned at 286.0 and 289.2 eV are assigned to carbon species from C-NH₂ and C-O groups at the edge of g-C₃N₄. In the case of the PW₁₂/g-C₃N₄-3.2 film, the aforementioned four characteristic peaks are still found. Three main peaks positioned at 398.2, 399.2 and 400.5 eV appear in the N 1s deconvoluted spectra of the starting g-C₃N₄ powder and PW₁₂/g-C₃N₄-3.2 film (Fig. 2b), which are assigned to pyridinic nitrogen (bonded to two neighboring carbons, C-N=C), graphitic nitrogen (bonded to three neighboring carbons, N-(C)₃) and nitrogen from C-NH₂ groups, respectively [62]. Two contributions at 37.1 (W 4f_{5/2}) and 35.0 eV (W 4f_{7/2}) are found in the W 4f deconvoluted spectrum of the PW₁₂/g-C₃N₄-3.2 film (Fig. 2c), which are the characteristic of W(VI) oxidation state of the Keggin unit [63], however, compared with the starting H₃PW₁₂O₄₀ (binding energies of W 4f_{5/2} and W 4f_{7/2} are 37.9 and 35.8 eV), the negative shifts of the binding energies are found, implying that chemical interactions exist between g-C₃N₄ and the Keggin unit at the interface of both components [64].

3.1.2. Optical absorption properties

The optical absorption properties of the starting g-C₃N₄ nanosheets and H₃PW₁₂O₄₀ as well as g-C₃N₄ film and PW₁₂/g-C₃N₄ films are characterized by UV-vis/DRS. As shown in Fig. 3a, g-C₃N₄ nanosheets display a typical semiconductor optical absorption with edge at ca. 446 nm, attributing to the charge transfer from VB populated by N 2p orbitals to CB formed by C 2p orbitals [65]. Compared with g-C₃N₄ nanosheets, slight blueshift of the absorption edge (ca. 436 nm) is observed for the g-C₃N₄ film, which is ascribed to the interference of the included small amount of silica. As for the starting H₃PW₁₂O₄₀, it shows light absorption before 411 nm, corresponding to the charge transfer from O 2p to W 5d electronic states occurred at W-O_{b/c}-W bridge bonds [66]. Compared with g-C₃N₄ film, somewhat blueshift of the

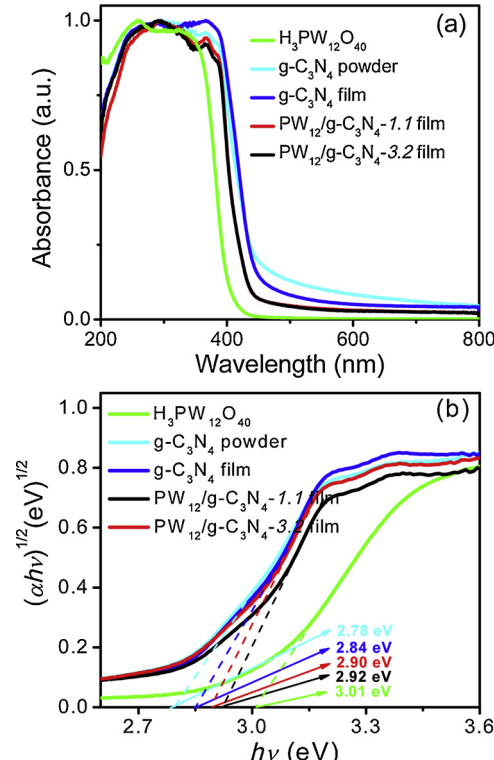


Fig. 3. The normalized UV-vis DRS (a) and Tauc plots (b) of the starting H₃PW₁₂O₄₀ and various g-C₃N₄-based materials.

absorption edges of the PW₁₂/g-C₃N₄-1.1 (427 nm) and PW₁₂/g-C₃N₄-3.2 films (424 nm) implies that the Keggin units indeed are introduced to g-C₃N₄. The band gaps of the above samples are determined from

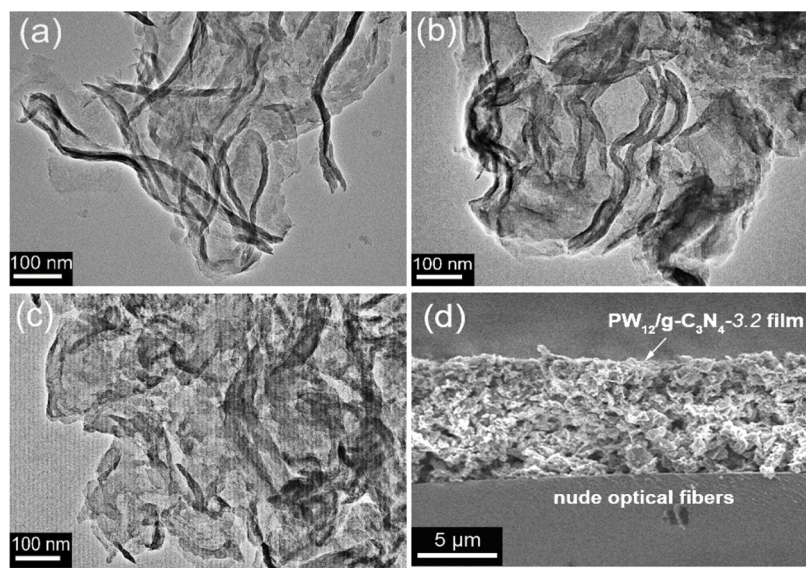


Fig. 4. TEM images of $\text{g-C}_3\text{N}_4$ powder (a), $\text{g-C}_3\text{N}_4$ film (b), $\text{PW}_{12}/\text{g-C}_3\text{N}_4$ -3.2 film (c) and cross-sectional SEM image of $\text{PW}_{12}/\text{g-C}_3\text{N}_4$ -3.2 film (d).

Tauc plots based on Tauc formula:

$$(\alpha h\nu)^{1/n} = A(h\nu - E_g)$$

In this formula, α , A , $h\nu$ and E_g represent the absorption coefficient, proportionality constant, Planck constant, light frequency and bandgap, respectively [67]. For $\text{g-C}_3\text{N}_4$ -based materials, $n = 2$, and it represents the indirect allowed transition [68]. From the tangent line of plots, extrapolated to the $h\nu$ axis intercept, the estimated E_g values of $\text{H}_3\text{PW}_{12}\text{O}_{40}$, $\text{g-C}_3\text{N}_4$ nanosheets, $\text{g-C}_3\text{N}_4$ film, $\text{PW}_{12}/\text{g-C}_3\text{N}_4$ -1.1 film and $\text{PW}_{12}/\text{g-C}_3\text{N}_4$ -3.2 film are 3.01, 2.78, 2.84, 2.90 and 2.92 eV, respectively (Fig. 3b).

3.1.3. Morphological characteristics and porosity properties

The corrugated, transparent and ultrathin sheet-like nanostructures of as-prepared $\text{g-C}_3\text{N}_4$ powder (Fig. 4a) and film (Fig. 4b) can be visibly observed by TEM images. After the introduction of $\text{H}_3\text{PW}_{12}\text{O}_{40}$, the primary ultrathin sheet-like nanostructure remains intact for the resulting $\text{PW}_{12}/\text{g-C}_3\text{N}_4$ -3.2 film (Fig. 4c); however, it is difficult to find out the $\text{H}_3\text{PW}_{12}\text{O}_{40}$ nanoparticles in this image. SEM observation for the $\text{PW}_{12}/\text{g-C}_3\text{N}_4$ -3.2 film-coated optical fibers reveals that the film is smooth with well-distributed $\text{H}_3\text{PW}_{12}\text{O}_{40}/\text{g-C}_3\text{N}_4$ nanoparticles on the surface, and the estimated film thickness is 8 μm for 7 layers (Fig. 4d).

Four samples including $\text{g-C}_3\text{N}_4$ powder, $\text{g-C}_3\text{N}_4$ film, $\text{PW}_{12}/\text{g-C}_3\text{N}_4$ -1.1 film and $\text{PW}_{12}/\text{g-C}_3\text{N}_4$ -3.2 film all exhibit a type IV isotherm, and their hysteresis loops (type H3) appear at high relative pressure region,

i.e., $P/P_0 = 0.65\text{--}0.97$ for $\text{g-C}_3\text{N}_4$ powder and $0.40\text{--}0.99$ for three $\text{g-C}_3\text{N}_4$ -based films (Fig. 5a), reflecting their larger and slit-like pores. Therefore, a slit nonlocal density functional theory (NLDFT) model is applied to analyze the pore size distribution of the samples. As shown in Fig. 5b, pure $\text{g-C}_3\text{N}_4$ power display broad pore size distribution centering at 8, 10 and 13–60 nm. The smaller pores with narrower pore-size distribution are induced by self-activation of urea during the thermal polymerization process, and the released NH_3 and CO_2 gases can act as the soft template; the larger pores with broader pore-size distribution are caused mainly by irregular stacking of sheet-like $\text{g-C}_3\text{N}_4$ nanosheets. The above pores can also be observed in the three $\text{g-C}_3\text{N}_4$ -based films; moreover, some micropores centering at 1.3 nm are also found, regardless of the presence of the Keggin unit or not. The micropores of the tested $\text{g-C}_3\text{N}_4$ -based films are therefore created by the included silica. The unique hierarchically structure renders the $\text{g-C}_3\text{N}_4$ film ($90.4 \text{ m}^2 \text{ g}^{-1}$) remarkably enlarged BET surface area as compared with $\text{g-C}_3\text{N}_4$ powder ($43.2 \text{ m}^2 \text{ g}^{-1}$). As for the $\text{PW}_{12}/\text{g-C}_3\text{N}_4$ -1.1 ($84.8 \text{ m}^2 \text{ g}^{-1}$) and $\text{PW}_{12}/\text{g-C}_3\text{N}_4$ -3.2 ($76.1 \text{ m}^2 \text{ g}^{-1}$) films, slightly decreased BET surface area compared with $\text{g-C}_3\text{N}_4$ film is ascribed to partial pore blockage of $\text{g-C}_3\text{N}_4$ film by the introduced Keggin units.

3.2. Photocatalytic removal of aromatics over the $\text{PW}_{12}/\text{g-C}_3\text{N}_4$ film-coated optical fibers

Light insensitive aromatics including benzene, toluene and *m*-xylene

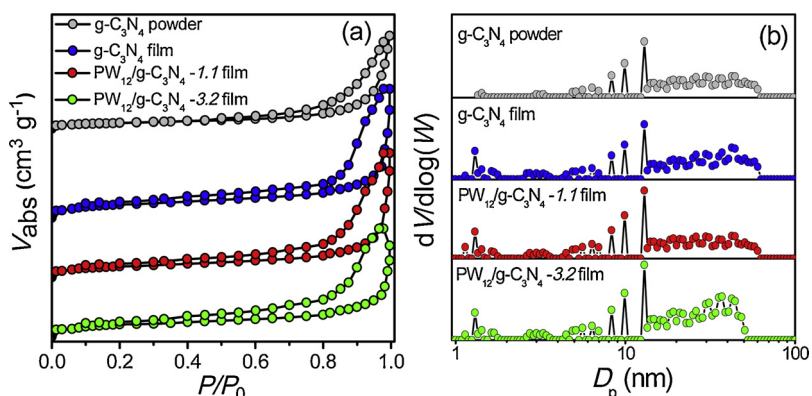


Fig. 5. Nitrogen gas adsorption-desorption isotherms (a) and pore size distribution curves obtained by a slit NLDFT model (b) of $\text{g-C}_3\text{N}_4$ powder/film as well as the $\text{PW}_{12}/\text{g-C}_3\text{N}_4$ films.

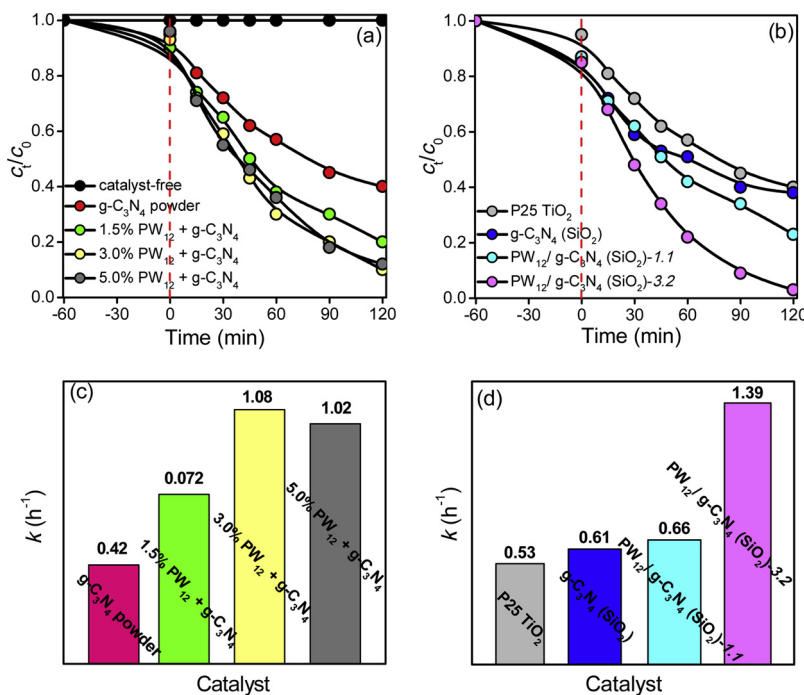


Fig. 6. Liquid-phase photocatalytic removal efficiency of *m*-xylene ($c_0 = 10 \text{ mg L}^{-1}$) over the simulated sunlight irradiated $\text{H}_3\text{PW}_{12}\text{O}_{40}$ and $\text{g-C}_3\text{N}_4$ powder (a) as well as $\text{PW}_{12}/\text{g-C}_3\text{N}_4(\text{SiO}_2)$ powders (b). The corresponding apparent rate constants (k) for *m*-xylene removal (c and d). Volume 50 mL; catalyst amount 50 mg.

are selected as the target pollutants to study the simulated sunlight photocatalytic performance of the $\text{PW}_{12}/\text{g-C}_3\text{N}_4$ film-coated optical fibers. Owing to structural stability and narrow UV light absorption with edge at 230 nm, it is a severe challenge to remove these typical volatile aromatics effectively by photocatalysis, especially under visible/solar light irradiation.

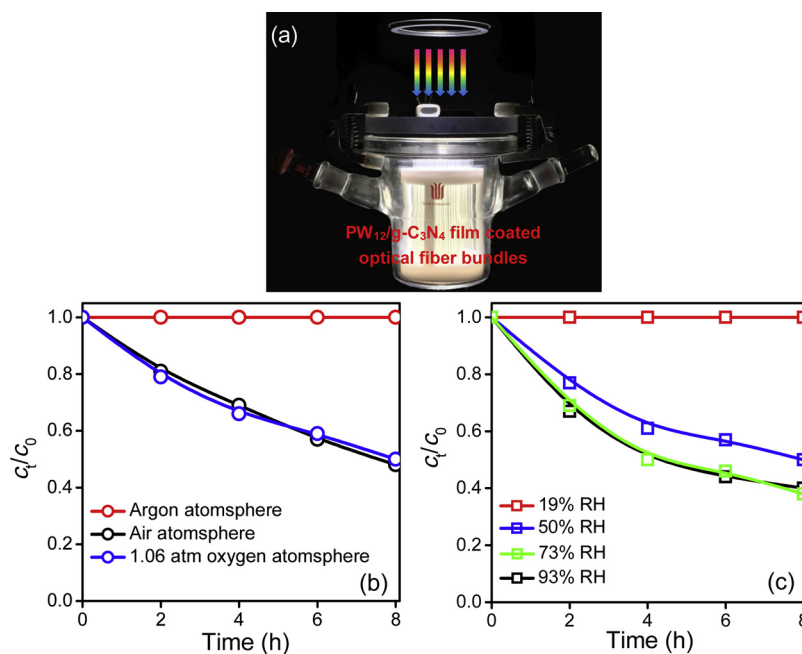
3.2.1. Photocatalytic removal efficiency

In order to explore the contribution of $\text{H}_3\text{PW}_{12}\text{O}_{40}$ to the photo-oxidation ability of $\text{g-C}_3\text{N}_4$ as well as to find out the optimal $\text{H}_3\text{PW}_{12}\text{O}_{40}$ loading for the preparation of $\text{PW}_{12}/\text{g-C}_3\text{N}_4$ film-coated quartz fibers, simulated sunlight photocatalytic removal of aromatics is firstly carried out in the liquid-phase (acetone/water, 1/1, v/v) by selecting *m*-xylene as the representative pollutant and $\text{g-C}_3\text{N}_4$ powder as the catalyst in the presence of $\text{H}_3\text{PW}_{12}\text{O}_{40}$, in which the weight percentage of $\text{H}_3\text{PW}_{12}\text{O}_{40}$ with respect to total amount of $\text{g-C}_3\text{N}_4$ and $\text{H}_3\text{PW}_{12}\text{O}_{40}$ is 1.5, 3.0 and 5.0%, respectively. In this system, $\text{H}_3\text{PW}_{12}\text{O}_{40}$ is homogeneous. As shown in Fig. 6a, the adsorption-desorption equilibrium between *m*-xylene and $\text{g-C}_3\text{N}_4$ powder reaches after stirring the suspension including the catalyst powder and aqueous *m*-xylene in dark for 60 min, and $\text{g-C}_3\text{N}_4$ powder exhibits very low absorption capacity towards *m*-xylene (< 10%). In the catalyst-free system, degradation of *m*-xylene hardly occurs. Remarkable degradation of *m*-xylene is observed under the simulated sunlight irradiating $\text{g-C}_3\text{N}_4$ powder or $\text{g-C}_3\text{N}_4$ powder and homogeneous $\text{H}_3\text{PW}_{12}\text{O}_{40}$; moreover, *m*-xylene removal efficiency is obviously enhanced after the addition of $\text{H}_3\text{PW}_{12}\text{O}_{40}$ in comparison of solitary $\text{g-C}_3\text{N}_4$ powder. Additionally, changing weight percentage of $\text{H}_3\text{PW}_{12}\text{O}_{40}$ from 1.5 to 3.0%, *m*-xylene removal efficiency increases gradually, and further increasing the weight percentage to 5.0%, the removal efficiency maintains unchangeable basically. For example, after simulated sunlight irradiating for 120 min, *m*-xylene removal efficiency is 60.1 ($\text{g-C}_3\text{N}_4$ powder), 80.3 (1.5% PW_{12} and $\text{g-C}_3\text{N}_4$ powder), 90.1 (3.0% PW_{12} and $\text{g-C}_3\text{N}_4$ powder) and 88.2% (5.0% PW_{12} and $\text{g-C}_3\text{N}_4$ powder), respectively. Therefore, $\text{H}_3\text{PW}_{12}\text{O}_{40}$ loading of 3.0% is enough to obtain significantly enhanced *m*-xylene removal efficiency.

Subsequently, the photocatalytic removal efficiency of *m*-xylene

over the $\text{g-C}_3\text{N}_4(\text{SiO}_2)$ and $\text{PW}_{12}/\text{g-C}_3\text{N}_4(\text{SiO}_2)$ powders is tested. The $\text{g-C}_3\text{N}_4(\text{SiO}_2)$ and $\text{PW}_{12}/\text{g-C}_3\text{N}_4(\text{SiO}_2)$ powders are prepared by drying suspension of $\text{g-C}_3\text{N}_4(\text{SiO}_2)$ and $\text{PW}_{12}/\text{g-C}_3\text{N}_4(\text{SiO}_2)$. As displayed in Fig. 6b, owing to the presence of a small amount of silica, $\text{g-C}_3\text{N}_4(\text{SiO}_2)$ and $\text{PW}_{12}/\text{g-C}_3\text{N}_4(\text{SiO}_2)$ powder possess larger BET surface area and thereby somewhat higher absorption capacity towards *m*-xylene (ca. 15%) as compared with $\text{g-C}_3\text{N}_4$ powder. Additionally, the above catalysts follow the activity order of $\text{g-C}_3\text{N}_4(\text{SiO}_2) < \text{PW}_{12}/\text{g-C}_3\text{N}_4(\text{SiO}_2)-1.1 < \text{PW}_{12}/\text{g-C}_3\text{N}_4(\text{SiO}_2)-3.2$. For instance, after simulated sunlight irradiating for 120 min, the removal efficiency of *m*-xylene is 62.5 [$\text{g-C}_3\text{N}_4(\text{SiO}_2)$], 77.2 [$\text{PW}_{12}/\text{g-C}_3\text{N}_4(\text{SiO}_2)-1.1$] and 97.4% [$\text{PW}_{12}/\text{g-C}_3\text{N}_4(\text{SiO}_2)-3.2$], respectively. Under the same conditions, the removal efficiency of *m*-xylene over P25 TiO_2 is 55.1%. Therefore, all tested $\text{g-C}_3\text{N}_4$ -based photocatalysts exhibit higher activity than that of P25 TiO_2 . It is noted that under the similar $\text{H}_3\text{PW}_{12}\text{O}_{40}$ loading (ca. 3.0%), $\text{PW}_{12}/\text{g-C}_3\text{N}_4(\text{SiO}_2)-3.2$ powder catalyst exhibits higher photocatalytic *m*-xylene removal efficiency than homogenous 3.0% PW_{12} and $\text{g-C}_3\text{N}_4$ (97.4% vs. 90.1%). On the one hand, $\text{PW}_{12}/\text{g-C}_3\text{N}_4(\text{SiO}_2)-3.2$ has larger BET surface area so that more active species are provided; more importantly, acid-base interaction between the Keggin unit and $\text{g-C}_3\text{N}_4$ at the interface of both components ensure their intimate interfacial contact, which boosts the interfacial charge carrier separation and migration and finally delays their recombination.

The reaction kinetics of *m*-xylene removal over the simulated sunlight irradiated various $\text{g-C}_3\text{N}_4$ -based photocatalysts in the liquid-phase are then studied (Fig. S2). As shown in Fig. S2a and b, each plot of $\ln(c_t/c_0)$ vs. t exhibits a good linearity, suggesting that *m*-xylene removal reaction follows pseudo-first-order kinetics. In homogeneous $\text{H}_3\text{PW}_{12}\text{O}_{40}$ and $\text{g-C}_3\text{N}_4$ powder systems, the determined apparent rate constant (k) for *m*-xylene removal over 3.0% PW_{12} and $\text{g-C}_3\text{N}_4$ (1.08 h^{-1}) is 2.57, 1.50 and 1.05 times higher than that of the starting $\text{g-C}_3\text{N}_4$ (0.42 h^{-1}), 1.5% PW_{12} and $\text{g-C}_3\text{N}_4$ (0.72 h^{-1}) and 5.0% PW_{12} and $\text{g-C}_3\text{N}_4$ (1.02 h^{-1}), respectively (Fig. 6c). In heterogeneous $\text{PW}_{12}/\text{g-C}_3\text{N}_4(\text{SiO}_2)$ systems, k value for *m*-xylene removal over the $\text{PW}_{12}/\text{g-C}_3\text{N}_4(\text{SiO}_2)-3.2$ catalyst (1.39 h^{-1}) is 2.62, 2.27 and 2.10 times higher than that of P25 TiO_2 (0.53 h^{-1}), $\text{g-C}_3\text{N}_4(\text{SiO}_2)$ (0.61 h^{-1}) and $\text{PW}_{12}/\text{g-C}_3\text{N}_4(\text{SiO}_2)-1.1$ (0.66 h^{-1}), respectively (Fig. 6d). The results indicate



that the formation of the PW₁₂/g-C₃N₄ composites can significantly enhance the photocatalytic oxidation rate of g-C₃N₄ to *m*-xylene.

On the basis of the above studies, gas-phase photocatalytic removal of aromatics including benzene, toluene and *m*-xylene over the PW₁₂/g-C₃N₄ film-coated optical fiber is subsequently investigated in a custom-designed quartz reactor (Fig. 7a), and g-C₃N₄ film-coated optical fibers are also tested under the identical conditions.

At first, influence of the important operating parameters including the concentration of oxygen and RH on the removal efficiency of gaseous aromatics is studied by selecting the PW₁₂/g-C₃N₄-1.1 film-coated optical fibers as the representative photocatalyst and *m*-xylene as the pollutant. As shown in Fig. 7b, the removal of a gaseous *m*-xylene is restrained totally in argon atmosphere (RH of 50%). Otherwise, remarkable decrease of the concentration of *m*-xylene is observed when the reaction takes place under air atmosphere or 1.06 atm oxygen atmosphere. For example, after the simulated sunlight irradiating the PW₁₂/g-C₃N₄-1.1 film for 8 h, *m*-xylene removal efficiency reaches to ca. 50.0% in both cases. The above result suggests that oxygen is indispensable to remove gaseous *m*-xylene under simulated sunlight irradiating the PW₁₂/g-C₃N₄-1.1 film. This is due to the fact that oxygen behaves as the e_{CB}⁻ trapping agent to form ·O₂⁻ radicals, one of the most important active species that are responsible for the oxidation of *m*-xylene [69]. The result also indicates that oxygen provided by air is sufficient for the target reaction.

RH of the system is another important operating parameter that dominates the photocatalytic removal efficiency of *m*-xylene. As shown in Fig. 7c, at extremely low RH (19%), the removal of gaseous *m*-xylene is inhibited completely, while gradually enhanced *m*-xylene removal efficiency is found as increasing RH to 50 and 73%, respectively. For example, *m*-xylene removal efficiency reaches 50.2 and 62.4% at RH of 50 and 73%, respectively, after the simulated sunlight irradiating the PW₁₂/g-C₃N₄-1.1 film for 8 h. At much higher RH (93%), *m*-xylene removal efficiency (58.9%, 8 h) decreases slightly. The above result implies that water vapor has contradictory effect on the photocatalytic removal of gaseous *m*-xylene. On the one hand, water is essential because it can provide OH⁻ ions to react with h_{VB}⁺ to yield surface-bound ·OH radical, one of the active oxygen species with strong oxidation ability that is responsible for deep oxidation of *m*-xylene; in addition, the recombination opportunity of h_{VB}⁺ and e_{CB}⁻ is therefore reduced owing to the consumption of h_{VB}⁺. On the other hand, much higher RH (e.g., 93%) leads to more water molecules adsorbed on the

Fig. 7. (a) Custom-made PW₁₂/g-C₃N₄ film-coated optical fiber photoreactor (300 mL) for gas-phase photocatalytic removal of aromatics. Influence of the concentration of oxygen (b) and RH (c) on the photocatalytic removal efficiency of *m*-xylene over the PW₁₂/g-C₃N₄-1.1 film. Catalyst amount 135 mg; *c*₀ = 9.8 mg L⁻¹; volume 300 mL; 320 nm < λ < 680 nm.

surface of the PW₁₂/g-C₃N₄-1.1 film, which prevents hydrophobic *m*-xylene molecule from adsorption on the catalyst surface, giving rise to somewhat decreased *m*-xylene removal efficiency due to the reduced contact opportunity of the substrate with the active species [1]. Therefore, an optimal RH of 73% is set for subsequent gas-phase photocatalytic removal of aromatics. It should be noted that the above results also provide an indirect evidence of the generation of ·O₂⁻ and ·OH radicals in current photocatalytic system.

At RH of 73% and air atmosphere, gas-phase photocatalytic removal of benzene, toluene and *m*-xylene (*c*₀ = 6.0 mg L⁻¹) over the simulated sunlight irradiated g-C₃N₄ film, PW₁₂/g-C₃N₄-1.1 film and PW₁₂/g-C₃N₄-3.2 film are studied. In the absence of the catalyst, the concentrations of these three pollutants retain unchangeable after 8 h light irradiation, reflecting that direct photolysis is inactive for their decomposition. In the presence of both catalyst and simulated sunlight, obvious removal of gaseous benzene, toluene and *m*-xylene is found, and the tested film catalysts follow the activity order of g-C₃N₄ film < PW₁₂/g-C₃N₄-1.1 film < PW₁₂/g-C₃N₄-3.2 film. For instance, after simulated sunlight irradiating for 8 h, benzene removal efficiency reaches 54.2 (g-C₃N₄ film), 70.0 (PW₁₂/g-C₃N₄-1.1 film) and 84.3% (PW₁₂/g-C₃N₄-3.2 film), respectively (Fig. 8a); toluene removal efficiency is 60.9 (g-C₃N₄ film), 89.1 (PW₁₂/g-C₃N₄-1.1 film) and 98.3% (PW₁₂/g-C₃N₄-3.2 film), respectively (Fig. 8b); *m*-xylene removal efficiency reaches 62.1 (g-C₃N₄ film), 84.3 (PW₁₂/g-C₃N₄-1.1 film) and 95.6% (PW₁₂/g-C₃N₄-3.2 film), respectively (Fig. 8c).

The gas-phase photocatalytic removal of benzene, toluene and *m*-xylene at lower initial concentration (*c*₀ = 1.0 mg L⁻¹) over the PW₁₂/g-C₃N₄-3.2 film-coated optical fibers is also tested. As shown in Fig. S3, the PW₁₂/g-C₃N₄-3.2 film still displays the excellent photocatalytic oxidation ability to three gaseous aromatics at lower initial concentration, and benzene, toluene and *m*-xylene removal efficiency reaches 90.3, 100.0 and 97.5%, respectively, after simulated sunlight irradiating for 8 h.

The reaction kinetics of gas-phase photocatalytic removal of benzene, toluene and *m*-xylene over the simulated sunlight irradiated various g-C₃N₄-based film catalysts are also studied. As shown in Fig. S2c-e, the plots of ln(*c*/*c*₀) vs. *t* exhibit good linearity, implying that the target reactions follow pseudo-first-order kinetics. From the determined apparent rate constants summarized in Fig. 8d it can be seen: i) *k* value for benzene removal over the simulated sunlight irradiated PW₁₂/g-C₃N₄-3.2 film (0.080 h⁻¹) is 1.78 and 2.42 times higher than that of

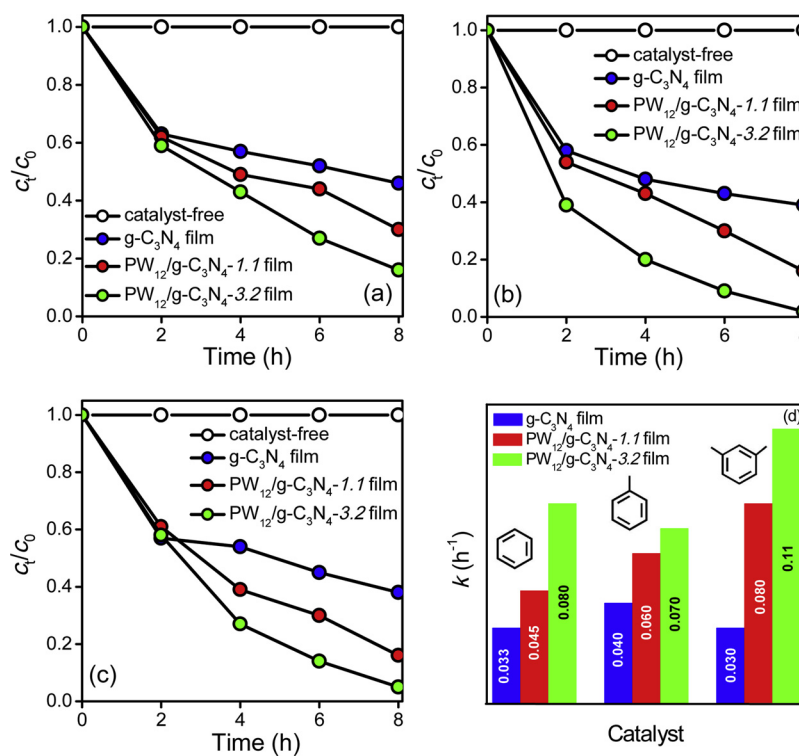


Fig. 8. Gas-phase photocatalytic removal efficiency of benzene (a), toluene (b) and *m*-xylene (c) over the simulated sunlight irradiated $g\text{-C}_3\text{N}_4$ film, $PW_{12}/g\text{-C}_3\text{N}_4\text{-1.1}$ film and $PW_{12}/g\text{-C}_3\text{N}_4\text{-3.2}$ film. The corresponding apparent rate constants (k) for benzene, toluene and *m*-xylene removal (d). $c_0 = 6.0 \text{ mg L}^{-1}$; RH = 73%; Air; Catalyst amount 135 mg; volume 300 mL.

$PW_{12}/g\text{-C}_3\text{N}_4\text{-1.1}$ film (0.045 h^{-1}) and $g\text{-C}_3\text{N}_4$ film (0.033 h^{-1}); ii) k value for toluene removal over the simulated sunlight irradiated $PW_{12}/g\text{-C}_3\text{N}_4\text{-3.2}$ film (0.070 h^{-1}) is 1.17 and 1.75 times higher than that of $PW_{12}/g\text{-C}_3\text{N}_4\text{-1.1}$ film (0.060 h^{-1}) and $g\text{-C}_3\text{N}_4$ film (0.040 h^{-1}); and iii) k value for *m*-xylene removal over the simulated sunlight irradiated $PW_{12}/g\text{-C}_3\text{N}_4\text{-3.2}$ film (0.11 h^{-1}) is 1.38 and 3.67 times higher than that of $PW_{12}/g\text{-C}_3\text{N}_4\text{-1.1}$ film (0.080 h^{-1}) and $g\text{-C}_3\text{N}_4$ film (0.030 h^{-1}). The results confirm that the $PW_{12}/g\text{-C}_3\text{N}_4\text{-3.2}$ film exhibit the highest photocatalytic oxidation rate towards the target gaseous pollutants.

The mineralization ability is also a vital criterion to evaluate the photocatalytic performance, and it takes much longer time to mineralize the organic pollutants totally compared with their degradation. Herein, the mineralization ability of the representative $PW_{12}/g\text{-C}_3\text{N}_4\text{-3.2}$ film is evaluated *via* monitoring the yielded aliphatic acids by IC qualitatively and quantificationally after the gaseous samples are dissolved in dilute NaOH aqueous solution. As shown in Fig. S4a–c, succinic acid is identified during simulated sunlight photocatalytic oxidation of gaseous benzene, toluene and *m*-xylene over the $PW_{12}/g\text{-C}_3\text{N}_4\text{-3.2}$ film-coated optical fibers, implying cleavage of aromatic rings of the pollutants and their further mineralization. Changes of the concentration of succinic acid during the above process are presented in Fig. 9a, showing that continuous extending the light irradiation time leads to slowly decreased succinic acid concentration. Therefore, succinic acid is further decomposed to other aliphatic acids with smaller molecular weight. However, owing to considerably low initial concentration of gaseous aromatics, the produced aliphatic acids with smaller molecular weight such as acetic acid and formic acid are failed to be found in these systems. Additionally, in our gas-tight photoreactor, it is impossible to increase the initial concentration of gaseous aromatics significantly. Therefore, the mineralization ability of the $PW_{12}/g\text{-C}_3\text{N}_4\text{-3.2}$ film is further studied in the liquid-phase photocatalytic degradation of toluene ($c_0 = 50 \text{ mg L}^{-1}$). In this case, three aliphatic acids including succinic acid, acetic acid and formic acid are identified (Fig. S4d), originating from the cleavage of the aromatic rings of toluene molecules. The concentration changes of succinic acid, acetic acid and formic acid during the photocatalytic degradation process are monitored (Fig. 9b). With increasing light irradiation time, the

concentrations of formic acid and acetic acid increase gradually, suggesting unceasing mineralization of toluene.

3.2.2. Photocatalyst stability and recyclability

The adhesion of the coated $PW_{12}/g\text{-C}_3\text{N}_4$ film on the optical fibers as well as their stability and recyclability can be envisaged as a significant challenge for the potential applications in removal of gaseous pollutants. To assess these performances, gas-phase photocatalytic removal of benzene, toluene and *m*-xylene, respectively, is repeated for ten times over the representative $PW_{12}/g\text{-C}_3\text{N}_4\text{-3.2}$ film-coated optical fibers. After each catalytic run, the coated $PW_{12}/g\text{-C}_3\text{N}_4\text{-3.2}$ film is firstly washed with 0.1% (v/v) H_2O_2 under simulated sunlight irradiation to remove the adsorbed intermediates completely, and then the film is further washed with water for three times. After drying at 80 °C, the recovered catalyst-coated optical fibers are used for subsequent catalytic runs. As displayed in Fig. 10a, the removal efficiency of benzene, toluene and *m*-xylene is 84.3, 98.3 and 95.6% (1st), 83.2, 98.1 and 96.8% (2nd), 86.2, 97.0 and 93.4% (3rd), 83.8, 99.1 and 94.2% (4th), 81.9, 96.1 and 96.5% (5th), 80.1, 98.5 and 94.5% (6th), 81.4, 98.3 and 96.5% (7th), 87.3, 97.2 and 95.1% (8th), 84.0, 99.2 and 95.1% (9th) and 83.9, 97.6 and 97.7% (10th), respectively, after the simulated sunlight irradiation for 8 h for each run. The result highlights the excellent adhesion, stability and recyclability of the $PW_{12}/g\text{-C}_3\text{N}_4$ film, and the activity loss is negligible after total thirty times' catalytic runs; additionally, the crystal phase structure, morphology and chemical structure of the 30th time used $PW_{12}/g\text{-C}_3\text{N}_4\text{-3.2}$ film remain intact, confirmed by XRD (Fig. 10b), TEM (Fig. 10c) and FT-IR analysis (Fig. 10d). The excellent stability and recyclability of the $PW_{12}/g\text{-C}_3\text{N}_4$ film is attributed to strong interactions between the Keggin units and $g\text{-C}_3\text{N}_4$ as well as silica framework, which significantly inhibits the drop of the Keggin unit from the $H_3PW_{12}O_{40}/g\text{-C}_3\text{N}_4$ film during aqueous solution washing (confirmed by ICP-AES); meanwhile, as-designed $PW_{12}/g\text{-C}_3\text{N}_4$ film coating technique is reasonable. Therefore, the $PW_{12}/g\text{-C}_3\text{N}_4$ film-coated optical fiber photoreactor shows potential for removal of highly toxic and refractory VOCs in a large scale.

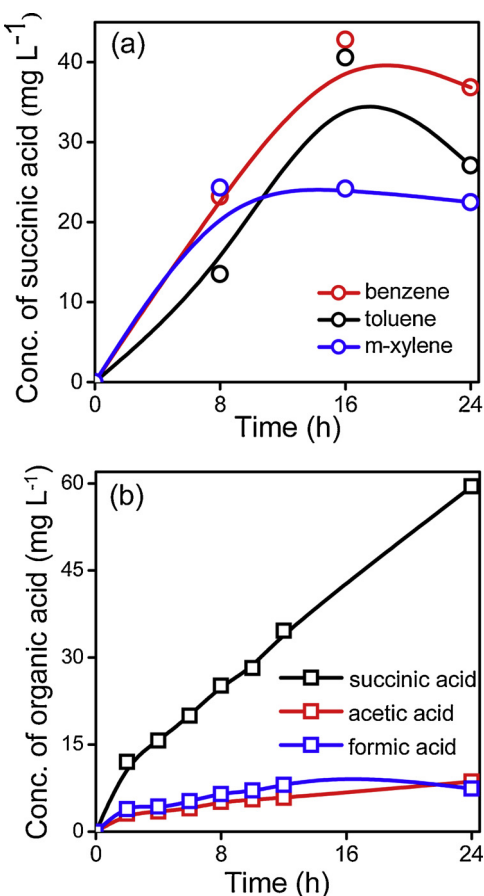


Fig. 9. Temporal evolutions of the concentrations of (a) succinic acid during the process of the PW₁₂/g-C₃N₄-3.2 film-photocatalyzed degradation of gaseous benzene, toluene and *m*-xylene ($c_0 = 6.0 \text{ mg L}^{-1}$) as well as (b) various organic acids during the process of the PW₁₂/g-C₃N₄-3.2 film-photocatalyzed degradation of an aqueous toluene ($c_0 = 50 \text{ mg L}^{-1}$). Catalyst amount 135 mg; volume 300 mL; $320 \text{ nm} < \lambda < 680 \text{ nm}$.

3.2.3. Photocatalytic activity interpretation and reaction mechanism considerations

To explore the origins of the enhanced gas-phase photocatalytic removal efficiency of aromatics over the PW₁₂/g-C₃N₄ with respect to g-C₃N₄, a series of tests including DMPO spin-trapping ESR, transient photocurrent responses and photocatalytic reduction of Cr(VI) are carried out.

At first, the generated active oxygen species in the simulated sunlight irradiated g-C₃N₄ powder, H₃PW₁₂O₄₀ as well as PW₁₂/g-C₃N₄ film systems are identified by DMPO spin-trapping ESR measurements in aqueous dispersion for DMPO-·OH adduct and methanol dispersion for DMPO-·O₂⁻ adduct. As displayed in Fig. 11a, no ESR signals of DMPO-·OH adduct are detected in the dark. Under simulated sunlight irradiation, only weak characteristic signals related to DMPO-·OH adduct are observed in g-C₃N₄ system, suggesting that only small amount of ·OH radicals are generated in this system. However, obviously strong signals related to DMPO-·OH adduct with an intensity ratio of 1:2:2:1 are identified in the DMPO spin-trapping ESR spectrum of the PW₁₂/g-C₃N₄-1.1 film system [70], and the intensities of four characteristic signals of DMPO-·OH adduct remarkably increase as increasing PW₁₂ loading to 3.2%. The result indicates that more abundant ·OH radicals are generated after chemical bonding the Keggin units with g-C₃N₄. As displayed in Fig. 11b, no ESR signals of DMPO-·O₂⁻ adduct are found in the dark. Under simulated sunlight irradiation, the special DMPO spin-trapping ESR spectra of g-C₃N₄ powder and PW₁₂/g-C₃N₄ films in methanol dispersion with an intensity ratio of 1:1:1:1 quartet signals are clearly found, suggesting the formation of ·O₂⁻ radicals in both systems [71]; moreover, the intensities of the characteristic signals increase significantly as increasing PW₁₂ loading from 0, 1.1 to 3.2%. The result also signifies that more plentiful ·O₂⁻ radicals are formed after the introduction of the Keggin units to g-C₃N₄. However, ·O₂⁻ radicals are hardly identified in a pure H₃PW₁₂O₄₀ system under simulated sunlight irradiation, as confirmed by DMPO spin-trapping ESR spectra of H₃PW₁₂O₄₀ in methanol dispersion for DMPO-·O₂⁻ adduct (Fig. S5a).

It should be noted that in the catalyst-free systems some weak split peaks are observed in DMPO spin-trapping ESR spectra in aqueous dispersion for DMPO-·OH adduct (Fig. 11a) and methanol dispersion for DMPO-·O₂⁻ adduct (Fig. 11b) under Xe lamp irradiation, however, the peak positions of DMPO-Xe lamp are different from those originated from catalyst-Xe lamp; more importantly, the peak intensities of DMPO-

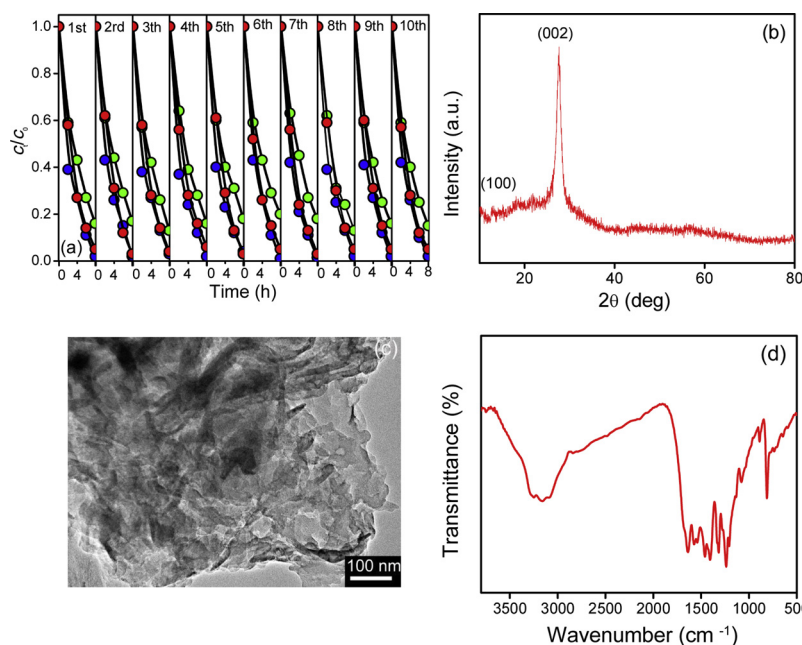


Fig. 10. (a) Reusability of the PW₁₂/g-C₃N₄-3.2 film in gas-phase photocatalytic removal of benzene (green symbol), toluene (blue symbol) and *m*-xylene (red symbol). $c_0 = 6.0 \text{ mg L}^{-1}$. XRD pattern (b), TEM image (c) and FT-IR spectra (d) of the 30th time used PW₁₂/g-C₃N₄-3.2 film. The first time used catalyst amount 135 mg; volume 300 mL; $320 \text{ nm} < \lambda < 680 \text{ nm}$ (For interpretation of the references to colour in this figure legend, the reader is referred to the web version of this article).

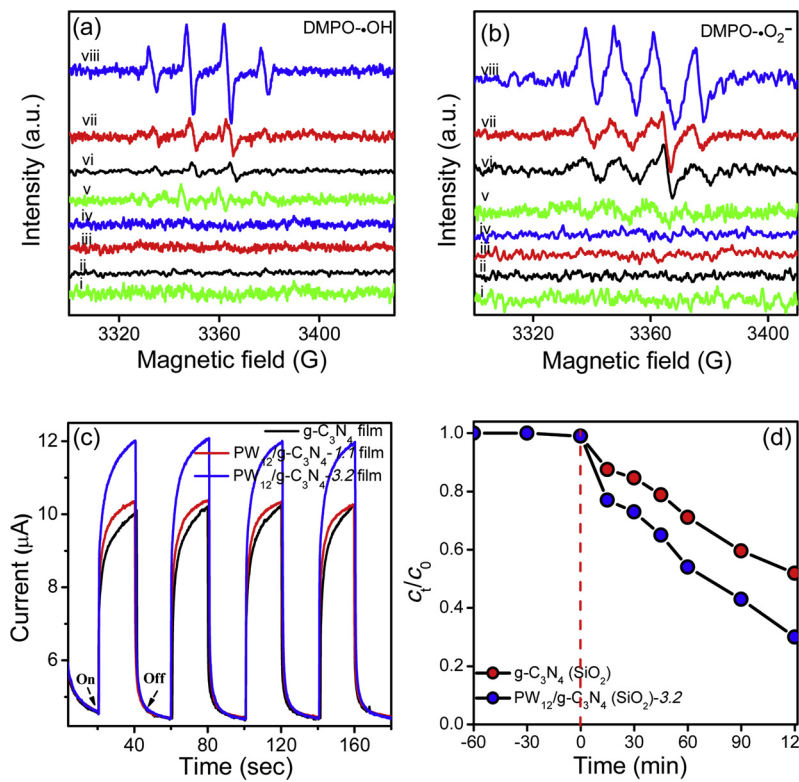
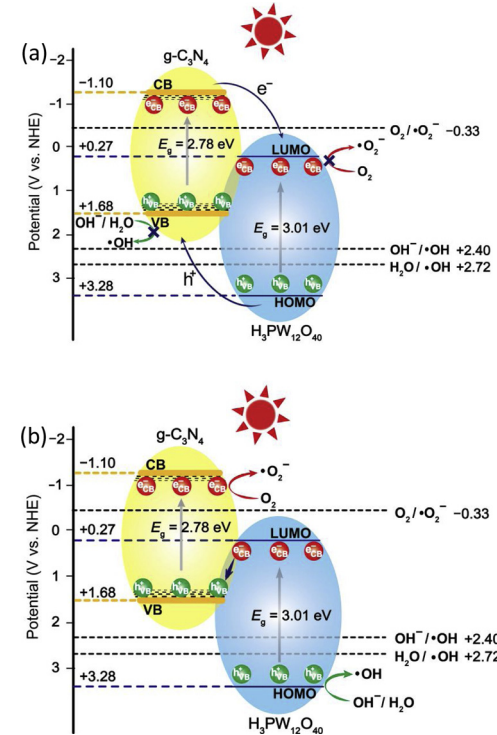


Fig. 11. DMPO spin-trapping ESR spectra of g-C₃N₄ and PW₁₂/g-C₃N₄ in aqueous dispersion for DMPO-·OH adduct (a) and methanol dispersion for DMPO-·O₂⁻ adduct (b). i. DMPO in dark; ii. g-C₃N₄ powder in dark; iii. PW₁₂/g-C₃N₄-1.1 film in dark; iv. PW₁₂/g-C₃N₄-3.2 film in dark; v. DMPO-Xe lamp; vi. g-C₃N₄ powder-Xe lamp; vii. PW₁₂/g-C₃N₄-1.1 film-Xe lamp; viii. PW₁₂/g-C₃N₄-3.2 film-Xe lamp. The transient photocurrent responses of various g-C₃N₄ film-based working electrodes (c). Photocatalytic reduction of Cr(VI) ($c_0 = 20 \text{ mg L}^{-1}$) over g-C₃N₄ (SiO₂) and PW₁₂/g-C₃N₄ (SiO₂)-3.2 powders. $320 \text{ nm} < \lambda < 680 \text{ nm}$; volume 100 mL; catalyst amount 100 mg (d).

Xe lamp are obviously weaker than those originated from catalyst-Xe lamp. Therefore, it is confirmed that ESR signals generated in Xe lamp irradiated PW₁₂/g-C₃N₄ photocatalytic systems are due to the DMPO-·OH and DMPO-·O₂⁻ adducts.

Subsequently, the separation and migration efficiency of the photogenerated charge carriers over the g-C₃N₄ and PW₁₂/g-C₃N₄ films is evaluated by transient photocurrent measurement. As shown in Fig. 11c, under the simulated sunlight irradiation, the photocurrent responses of g-C₃N₄ film, PW₁₂/g-C₃N₄-1.1 film and PW₁₂/g-C₃N₄-3.2 film are reproducible and stable during four on-off intermittent irradiation cycles, and three tested films follow the photocurrent order of g-C₃N₄ film < PW₁₂/g-C₃N₄-1.1 film < PW₁₂/g-C₃N₄-3.2 film; moreover, the photocurrent intensity of the PW₁₂/g-C₃N₄-3.2 film (12.0 μA) is approximately 1.2 times higher than that of pure g-C₃N₄ film (10.1 μA). The generation of photocurrent is originated from the migration of e_{CB}⁻, while h_{VB}⁺ flow to the interfacial region of the electrode and electrolyte and thereby the separation of e_{CB}⁻ and h_{VB}⁺. Accordingly, higher photocurrent response of the PW₁₂/g-C₃N₄ films than bare g-C₃N₄ film indicates their enhanced charge carrier separation and migration efficiency and longer lifetimes of e_{CB}⁻ and h_{VB}⁺ owing to the introduction of the Keggin units; moreover, the PW₁₂/g-C₃N₄ film with higher H₃PW₁₂O₄₀ doping level (3.2%) possesses stronger charge carrier separation and migration efficiency than that of the PW₁₂/g-C₃N₄ film with lower H₃PW₁₂O₄₀ doping level (1.1%).

The separation and migration efficiency of e_{CB}⁻ and h_{VB}⁺ in the PW₁₂/g-C₃N₄ photocatalytic system is one of the dominated factors that determines the photocatalytic activity, and conventional donor-acceptor (Type II) and direct Z-scheme mechanism are two possible charge carrier separation and migration pathways. If the PW₁₂/g-C₃N₄ heterojunction follows the donor-acceptor charge carrier separation and migration mechanism, e_{CB}⁻ in the CB of g-C₃N₄ will migrate to the LUMO of H₃PW₁₂O₄₀, while h_{VB}⁺ in the HOMO of H₃PW₁₂O₄₀ will transfer to the VB of g-C₃N₄ (Scheme 2a). The result would lead to accumulating a great deal of e_{CB}⁻ on LUMO of H₃PW₁₂O₄₀ and h_{VB}⁺ on the VB of g-C₃N₄. On the basis of the energy band structure of H₃PW₁₂O₄₀ and g-C₃N₄ (Scheme 2), the LUMO level of H₃PW₁₂O₄₀

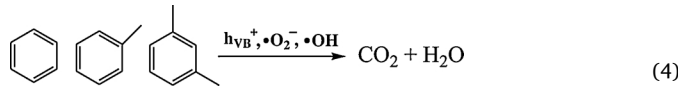
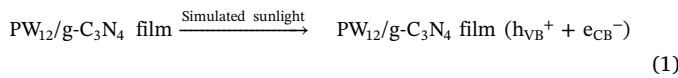


Scheme 2. Schematic illustration of energy band structures and two types of charge carrier separation and migration mechanism of the PW₁₂/g-C₃N₄ heterojunctions. (a) Donor-acceptor (Type II); (b) Z-scheme.

(0.27 V vs. NHE, determined by cyclic voltammogram method [72], Fig. S6a) is less negative than the redox potential of O₂/·O₂⁻ (-0.33 V vs. NHE) [67], and e_{CB}⁻ on the LUMO of H₃PW₁₂O₄₀ are hardly to reduce O₂ to ·O₂⁻ radicals directly; additionally, h_{VB}⁺ on the VB of g-C₃N₄ are unable to oxidize OH⁻/H₂O to ·OH radicals directly because VB edge

potential (E_{VB}) of $g\text{-C}_3\text{N}_4$ (1.68 V vs. NHE, calculated by combining with the E_g value and E_{CB} of $g\text{-C}_3\text{N}_4$) is less positive than the redox potential of OH^-/OH (2.40 V vs. NHE) or $\text{H}_2\text{O}/\text{OH}$ (2.72 V vs. NHE) [67]. The above Type II charge carrier separation and migration mechanism contradicts the results derived from DMPO spin-trapping ESR measurements in which abundant $\cdot\text{O}_2^-$ and $\cdot\text{OH}$ radicals are generated in the $\text{PW}_{12}/g\text{-C}_3\text{N}_4$ system. Additionally, small amount of $\cdot\text{OH}$ radicals generated in solitary $g\text{-C}_3\text{N}_4$ system is due to the multiple-electron reduction reaction of dioxygen by e_{CB}^- on the CB of $g\text{-C}_3\text{N}_4$ rather than direct oxidation reaction of $\text{OH}^-/\text{H}_2\text{O}$ by h_{VB}^+ on $g\text{-C}_3\text{N}_4$ [73].

Alternatively, since the CB edge potential of $g\text{-C}_3\text{N}_4$ (−1.10 V vs. NHE, determined by Mott-Schottky plot, Fig. S6b) is more negative than the redox potential of O_2/O_2^- , $\cdot\text{O}_2^-$ radical is able to generate *via* reduction of molecular oxygen by e_{CB}^- on the $g\text{-C}_3\text{N}_4$; additionally, the HOMO level of $\text{H}_3\text{PW}_{12}\text{O}_{40}$ (3.28 V vs. NHE, determined by VB XPS, Fig. S6c) is more positive than the redox potential of OH^-/OH or $\text{H}_2\text{O}/\text{OH}$, and $\cdot\text{OH}$ radical is therefore yielded *via* the oxidation of $\text{OH}^-/\text{H}_2\text{O}$ by h_{VB}^+ on the Keggin units. Therefore, a simulated sunlight-driven direct Z-scheme rather than conventional donor-acceptor charge carrier transformation path is proposed in the $\text{PW}_{12}/g\text{-C}_3\text{N}_4$ system. As illustrated in Scheme 2b and Eq. (1), under the simulated sunlight irradiating the $\text{PW}_{12}/g\text{-C}_3\text{N}_4$, $e_{CB}^- - h_{VB}^+$ pairs are generated. The well-matched energy band structures and intimate contact of the Keggin units with $g\text{-C}_3\text{N}_4$ facilitate the spontaneous migration of e_{CB}^- on the LUMO of the Keggin units to the VB of $g\text{-C}_3\text{N}_4$, and the migrated e_{CB}^- could further recombine with h_{VB}^+ on the VB of $g\text{-C}_3\text{N}_4$. The result leaves behind the e_{CB}^- and h_{VB}^+ in the CB of $g\text{-C}_3\text{N}_4$ and the HOMO of $\text{H}_3\text{PW}_{12}\text{O}_{40}$, respectively. Such an extraordinary Z-scheme-dictated charge carrier migration pathway not only improves the separation efficiency of $e_{CB}^- - h_{VB}^+$ pairs but also keeps a remarkably high redox ability by retaining a highly negative CB edge and a highly positive HOMO level. As a consequence, more abundant $\cdot\text{O}_2^-$ and $\cdot\text{OH}$ radicals are generated *via* reduction of dioxygen by e_{CB}^- (Eq. (2)) and oxidation of $\text{OH}^-/\text{H}_2\text{O}$ by h_{VB}^+ (Eq. (3)) as compared with the solitary $g\text{-C}_3\text{N}_4$ system. Under the attack of active species including h_{VB}^+ , $\cdot\text{O}_2^-$ and $\cdot\text{OH}$, the aromatic ring of benzene, toluene or *m*-xylene is destructed, and further deep oxidation leads to mineralization of the pollutants to CO_2 and H_2O (Eq. (4)).



On the basis of the above discussion, compared with $g\text{-C}_3\text{N}_4$, the enhanced photocatalytic activity after chemical bonding the Keggin units with $g\text{-C}_3\text{N}_4$ is originated from the extraordinary Z-scheme-dictated charge carrier separation and migration mechanism in the $\text{PW}_{12}/g\text{-C}_3\text{N}_4$ heterojunction, which not only improves the charge carrier separation and migration efficiency but also provides more abundant $\cdot\text{O}_2^-$ and $\cdot\text{OH}$ radicals for oxidation of aromatics.

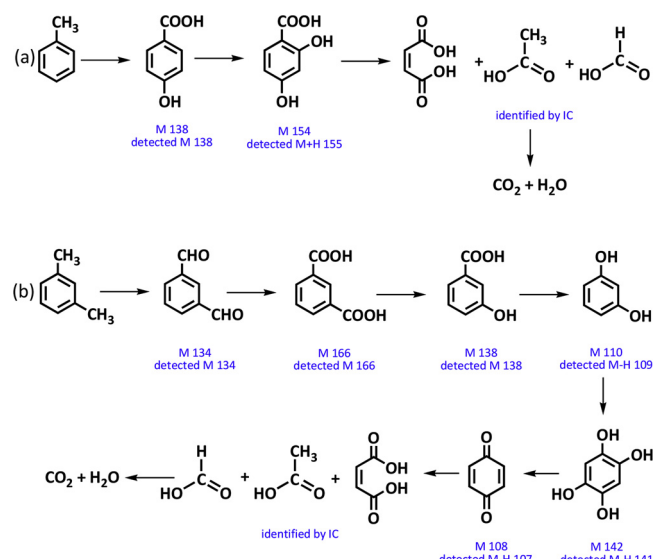
To further verify the proposed direct Z-scheme-dictated charge carrier migration mechanism of the $\text{PW}_{12}/g\text{-C}_3\text{N}_4$, the photocatalytic reduction ability of the $\text{PW}_{12}/g\text{-C}_3\text{N}_4$ (SiO_2)-3.2 powder is evaluated by reduction of aqueous highly toxic Cr(VI) to low toxic Cr(III). It is reported that the photocatalytic reduction of aqueous Cr(VI) is a proton assisted electron transfer reaction [74], accordingly, the reduction reaction performs at $\text{pH} = 2.68$. As shown in Fig. 11d, the $\text{PW}_{12}/g\text{-C}_3\text{N}_4$ (SiO_2)-3.2 still exhibits remarkably higher photocatalytic reduction ability to aqueous Cr(VI) than $g\text{-C}_3\text{N}_4$ (SiO_2), and the conversion of Cr (VI) reaches 70.0 [PW₁₂/g-C₃N₄ (SiO_2)-3.2] and 48.2% [g-C₃N₄ (SiO_2)], respectively, after 2 h simulated sunlight irradiation. The result is also

explained by Z-scheme-dictated charge carrier migration mechanism, which ensures e_{CB}^- remaining in the CB of $g\text{-C}_3\text{N}_4$ rather than migrating to the LUMO of the Keggin units and thereby the undiminished photocatalytic reduction ability. Additionally, the enhanced charge carrier separation and migration efficiency in current system gives rise to more e_{CB}^- to participate in the reduction of aqueous Cr(VI) to Cr(III), leading to the positive contribution to the enhanced photocatalytic reduction activity of the $\text{PW}_{12}/g\text{-C}_3\text{N}_4$ (SiO_2)-3.2.

Additionally, in as-designed quartz reactor, the $\text{PW}_{12}/g\text{-C}_3\text{N}_4$ film-coated optical fiber bundles are placed vertically throughout the reactor, which obviously increase the contact area of the catalyst film with the substrates; more importantly, optical fibers can deliver simulated sunlight to irradiate the $\text{PW}_{12}/g\text{-C}_3\text{N}_4$ film directly and uniformly without passing through the reaction medium [47,75]. Both factors ensure the increased light utilization efficiency of the catalyst, giving rise to the important contribution to the efficient gas-phase photocatalytic removal of aromatics.

Finally, to understand the photocatalytic reaction process deeply, LC-MS is applied to identify the reaction intermediates generated during the photocatalytic degradation of toluene (Fig. S7) and *m*-xylene (Fig. S8) over the $\text{PW}_{12}/g\text{-C}_3\text{N}_4$ -3.2 film. By the combination of the results of LC-MS and IC (Fig. S4) it is inferred that the degradation of toluene and *m*-xylene experiences main reaction pathway of hydroxylation of aromatic ring, further oxidation and aromatic ring opening. Namely, as shown in Fig. S7a and Scheme 3a, under the attack of the active species such as h_{VB}^+ , $\cdot\text{O}_2^-$ and $\cdot\text{OH}$ on the aromatic ring and methyl group, photocatalytic degradation of toluene over the $\text{PW}_{12}/g\text{-C}_3\text{N}_4$ -3.2 film firstly produces *p*-hydroxybenzoic acid, and further hydroxylation of *p*-hydroxybenzoic acid gives rise to 2,4-dihydroxybenzoic acid (Fig. S7b and Scheme 3a). Continuous oxidation results in aromatic ring opening, leading to a series of aliphatic acids such as succinic acid, acetic acid and formic acid. Eventually, deep oxidation of these aliphatic acids yields CO_2 and H_2O .

As shown in Fig. S8 and Scheme 3b, in photocatalytic degradation of *m*-xylene over the $\text{PW}_{12}/g\text{-C}_3\text{N}_4$ -3.2 film, *m*-xylene is firstly oxidized to isophthalaldehyde and then isophthalic acid by h_{VB}^+ , $\cdot\text{O}_2^-$ and $\cdot\text{OH}$. Successive decarbonylation from isophthalic acid leads to hydroxybenzoic acid and then *m*-dihydroxybenzene. Hydroxylation of *m*-dihydroxybenzene generates 1,2,4,5-tetrahydroxybenzene, and further oxidation of the latter yields benzoquinone. Benzoquinone suffers from ring opening reaction to yield a series of aliphatic acids. Ultimately, CO_2 and H_2O are produced after complete decomposition of *m*-xylene.



Scheme 3. Reaction pathway of simulated sunlight photocatalytic oxidation of toluene (a) and *m*-xylene (b) over the $\text{PW}_{12}/g\text{-C}_3\text{N}_4$.

4. Conclusions

The $H_3PW_{12}O_{40}/g\text{-}C_3N_4$ film-coated optical fibers are successfully demonstrated by a sol-gel combined with dip-withdrawing method, and they exhibit enhanced gas-phase photocatalytic removal efficiencies of benzene, toluene and *m*-xylene. Supported by the results of DMPO spin-trapping ESR measurement, transient photocurrent responses and photocatalytic reduction of Cr(VI), the well-matched energy band structures and intimate contact of the Keggin units and $g\text{-}C_3N_4$ suggest that the $H_3PW_{12}O_{40}/g\text{-}C_3N_4$ film catalysts follow a simulated sunlight-driven direct Z-scheme-dictated charge carrier transformation mechanism, which not only accelerates interfacial charge carrier separation but also leads to plentiful $\cdot O_2^-$ and $\cdot OH$ radicals involved in the reactions and thereby the enhanced photocatalytic activity; in addition, the increased contact area of the catalyst film with the substrates and the improved light harvesting also positively influence the activity of the $H_3PW_{12}O_{40}/g\text{-}C_3N_4$ film. The $H_3PW_{12}O_{40}/g\text{-}C_3N_4$ films also display excellent catalytic stability and reusability, attributing to strong interactions between the Keggin units and $g\text{-}C_3N_4$ as well as silica framework. Therefore, as-designed $H_3PW_{12}O_{40}/g\text{-}C_3N_4$ film-coated optical fiber photoreactor shows potential for removal of highly toxic and refractory VOCs in a large scale.

Acknowledgements

This work is supported by NSFC of China (21573038 and 51608102), and Jilin province science and technology development projects (20160520177JH).

Appendix A. Supplementary data

Supplementary material related to this article can be found, in the online version, at doi:<https://doi.org/10.1016/j.apcatb.2019.03.063>.

References

- [1] A.H. Mamaghani, F. Haghigheh, C.S. Lee, *Appl. Catal. B: Environ.* 203 (2017) 249–269.
- [2] D.S. Selishchev, N.S. Kolobov, A.A. Pershin, D.V. Kozlov, *Appl. Catal. B: Environ.* 200 (2017) 503–513.
- [3] Y.S. Won, J.W. Jeon, D.H. Lee, M.G. Lee, *J. Chem. Eng. Jpn.* 50 (2017) 589–594.
- [4] L.X. Zhong, F. Haghigheh, *Build. Environ.* 91 (2015) 191–203.
- [5] Y. Li, X.Y. Wu, J. Li, K. Wang, G.K. Zhang, *Appl. Catal. B: Environ.* 229 (2018) 218–226.
- [6] S. Weon, E. Choi, H. Kim, J.Y. Kim, H.J. Park, S. Kim, W. Kim, W. Choi, *Environ. Sci. Technol.* 52 (2018) 9330–9340.
- [7] V. Héquet, C. Raillard, O. Debono, F. Thévent, N. Locoge, L. Le Coq, *Appl. Catal. B: Environ.* 226 (2018) 473–486.
- [8] S. Weon, J. Kim, W. Choi, *Appl. Catal. B: Environ.* 220 (2018) 1–8.
- [9] J. Ji, Y. Xu, H.B. Huang, M. He, S.L. Liu, G.Y. Liu, R.J. Xie, Q.Y. Feng, Y.J. Shu, Y.J. Zhan, R.M. Fang, X.G. Ye, Dennis Y.C. Leung, *Chem. Eng. J.* 327 (2017) 490–499.
- [10] Batuira M. da Costa Filho, Ana L.P. Araujo, G.V. Silva, Rui A.R. Boaventura, Madalena M. Dias, José C.B. Lopes, Vítor J.P. Vilar, *Chem. Eng. J.* 310 (2017) 331–341.
- [11] S. Weon, J. Choi, T. Park, W. Choi, *Appl. Catal. B: Environ.* 205 (2017) 386–392.
- [12] W.J. Ong, L.L. Tan, Y.H. Ng, S.T. Yong, S.P. Chai, *Chem. Rev.* 116 (2016) 7159–7329.
- [13] C.M. Li, S.Y. Yu, H.J. Dong, C.B. Liu, H.J. Wu, H.N. Che, G. Chen, *Appl. Catal. B: Environ.* 238 (2018) 284–293.
- [14] K.S. Lakhi, D.H. Park, K. Al-Bahily, W. Cha, B. Viswanathan, J.H. Choy, A. Vinu, *Chem. Soc. Rev.* 46 (2017) 72–101.
- [15] S.C. Yan, Z.S. Li, Z.G. Zou, *Langmuir* 25 (2017) 10397–10491.
- [16] X.Q. Hao, J. Zhou, Z.W. Cui, Y.C. Wang, Y. Wang, Z.G. Zou, *Appl. Catal. B: Environ.* 229 (2018) 41–51.
- [17] B. Lin, H. Li, H. An, W.B. Hao, J.J. Wei, Y.Z. Dai, C.S. Ma, G.D. Yang, *Appl. Catal. B: Environ.* 220 (2018) 542–552.
- [18] E.Z. Liu, J.B. Chen, Y.N. Ma, J. Feng, J. Jia, J. Fan, X.Y. Hu, *J. Colloid Interface Sci.* 524 (2018) 313–324.
- [19] J.J. Wang, L. Tang, G.N. Zeng, Y.C. Deng, Y. Liu, L.F. Wang, Y.Y. Zhou, Z. Guo, J.L. Wang, C. Zhang, *Appl. Catal. B: Environ.* 209 (2017) 285–294.
- [20] Y.Z. Hong, Y.H. Jiang, C.S. Li, W.Q. Fan, X. Yan, M. Yan, W.D. Shi, *Appl. Catal. B: Environ.* 180 (2016) 663–673.
- [21] J.G. Yu, S.H. Wang, J.X. Low, W. Xiao, *Phys. Chem. Chem. Phys.* 15 (2013) 16883–16890.
- [22] B.C. Zhu, P.F. Xia, Y. Li, W.K. Ho, J.G. Yu, *Appl. Surf. Sci.* 391 (2017) 175–183.
- [23] Z.J. Xie, Y.P. Feng, F.L. Wang, D. Chen, Q.X. Zhang, Y.Q. Zeng, W.Y. Lv, G.G. Liu, *Appl. Catal. B: Environ.* 229 (2018) 96–104.
- [24] Z.Y. Liang, J.X. Wei, X. Wang, Y. Yu, F.X. Xiao, *J. Mater. Chem. A* 5 (2017) 15601–15612.
- [25] C.M. Li, S.Y. Yu, H.J. Dong, C.B. Liu, H.J. Wu, H.N. Che, G. Chen, *Appl. Catal. B: Environ.* 238 (2018) 284–293.
- [26] X.C. Wang, S.F. Blechert, M. Antonietti, *ACS Catal.* 2 (2012) 1596–1606.
- [27] Z.Y. Zhang, J.D. Huang, Y.R. Fang, M.Y. Zhang, K.C. Liu, B. Dong, *Adv. Mater.* 29 (2017) 1606688.
- [28] X.J. She, J.J. Wu, H. Xu, J. Zhong, Y. Wang, Y.H. Song, K.Q. Nie, Y. Liu, Y.C. Yang, M.T.F. Rodrigues, R. Vajtai, J. Lou, D. Du, H.M. Li, P.M. Ajayan, *Adv. Energy Mater.* 7 (2017) 1700025.
- [29] T.M. Di, B.C. Zhu, B. Cheng, J.G. Yu, J.S. Xu, *J. Catal.* 32 (2017) 532–541.
- [30] Z.F. Jiang, W.M. Wan, H.M. Li, S.Q. Yuan, H.J. Zhao, P.K. Wong, *Adv. Mater.* 30 (2018) 1706108.
- [31] F.Q. Zhou, J.C. Fan, Q.J. Xu, Y.L. Min, *Appl. Catal. B: Environ.* 201 (2017) 77–83.
- [32] Y. Gong, X. Quan, H.T. Yu, S. Chen, H.M. Zhao, *Appl. Catal. B: Environ.* 237 (2017) 947–956.
- [33] I.V. Kozhevnikov, *Chem. Rev.* 98 (1998) 171–198.
- [34] C.L. Hill, *J. Mol. Catal. A: Chem.* 262 (2007) 2–6.
- [35] Y.H. Guo, C.W. Hu, *J. Mol. Catal. A: Chem.* 262 (2007) 136–148.
- [36] S.S. Wang, G.Y. Yang, *Chem. Rev.* 115 (2015) 4893–4962.
- [37] J.S. Li, X.J. Sang, W.L. Chen, L.C. Zhang, Z.M. Zhu, T.Y. Ma, Z.M. Su, E.B. Wang, *ACS Appl. Mater. Interfaces* 7 (2015) 13714–13721.
- [38] X.F. Qian, D.T. Yue, Z.Y. Tian, M. Reng, Y. Zhu, M. Kan, T.Y. Zhang, Y.X. Zhao, *Appl. Catal. B: Environ.* 193 (2016) 16–21.
- [39] M. Pal, S. Bera, S. Sarkar, S. Jana, *RSC Adv.* 4 (2014) 1552–11563.
- [40] K. Li, Y.P. Tang, Y.N. Xu, Y.N. Huo, H.X. Li, J.P. Jia, *Appl. Catal. B: Environ.* 140–141 (2013) 179–188.
- [41] S.Y. Zhu, S.J. Liang, Y. Wang, X.Y. Zhang, F.Y. Li, H.X. Lin, Z.Z. Zhang, X.X. Wang, *Appl. Catal. B: Environ.* 187 (2016) 11–18.
- [42] Z.Y. Jiang, B.B. Huang, Z.Z. Lou, Z.Y. Wang, X.D. Meng, Y.Y. Liu, X.Y. Qin, X.Y. Zhang, Y. Dai, *Dalton Trans.* 43 (2014) 8170–8173.
- [43] S.Q. Zhang, L. Chen, H.B. Liu, W. Guo, Y.X. Yang, Y.H. Guo, M.X. Huo, *Chem. Eng. J.* 200–202 (2012) 300–309.
- [44] W.Y. Choi, J.Y. Ko, H. Park, J.S. Chung, *Appl. Catal. B: Environ.* 31 (2001) 209–220.
- [45] L. Lin, H.Y. Wang, P. Xu, *Chem. Eng. J.* 310 (2017) 389–398.
- [46] K. Baba, S. Bulou, P. Choquet, N.D. Boscher, *ACS Appl. Mater. Interfaces* 9 (2017) 13733–13741.
- [47] Y.X. Yang, L. Geng, Y.N. Guo, J.Q. Meng, Y.H. Guo, *Appl. Surf. Sci.* 425 (2017) 535–546.
- [48] K. Wei, K.X. Li, L.S. Yan, S.L. Luo, H.Q. Guo, Y.H. Dai, X.B. Luo, *Appl. Catal. B: Environ.* 222 (2018) 88–98.
- [49] Y.H. Guo, K.X. Li, X.D. Yu, J.H. Clark, *Appl. Catal. B: Environ.* 81 (2008) 182–191.
- [50] J. Wu, L.W. Liao, W.S. Yan, Y. Xue, Y.F. Sun, X. Yan, Y.X. Chen, Y. Xie, *ChemSusChem* 5 (2012) 1207–1212.
- [51] F. Dong, L.W. Wu, Y.J. Sun, M. Fu, Z.B. Wu, S.C. Lee, *J. Mater. Chem.* 21 (2011) 15171–15174.
- [52] L.F. Cui, Y.F. Liu, X.Y. Fang, C.C. Yin, S.S. Li, D. Sun, S.F. Kang, *Green Chem.* 20 (2018) 1354–1361.
- [53] H.F. Liu, H.J. Li, J.M. Lu, S. Zeng, M. Wang, N.C. Luo, S.T. Xu, F. Wang, *ACS Catal.* 8 (2018) 4761–4771.
- [54] H.T. Wei, Q. Zhang, Y.C. Zhang, Z.J. Yang, A.P. Zhu, D.D. Dionysiou, *Appl. Catal. A: Gen.* 521 (2016) 9–18.
- [55] Q.Y. Lin, L. Li, S.J. Liang, M.H. Liu, J.H. Bi, L. Wu, *Appl. Catal. B: Environ.* 163 (2015) 135–142.
- [56] K.X. Li, L.S. Yan, Z.X. Zeng, S.L. Luo, X.B. Luo, X.M. Liu, H.Q. Guo, Y.H. Guo, *Appl. Catal. B: Environ.* 156–157 (2014) 141–152.
- [57] X.L. Wang, W.Q. Fang, W.Q. Liu, Y. Jia, D.W. Jing, Y. Wang, L.Y. Yang, X.Q. Gong, Y.F. Yao, H.G. Yang, X.D. Yao, *J. Mater. Chem. A* 5 (2017) 19227–19236.
- [58] H.H. Ou, P.J. Yang, L.H. Lin, M. Anpo, X.C. Wang, *Angew. Chem. Int. Ed.* 56 (2017) 10905–10910.
- [59] D.Y. Song, S. An, Y.N. Sun, Y.H. Guo, *J. Catal.* 333 (2016) 184–199.
- [60] M. Peer, M. Lusardi, K.F. Jensen, *Chem. Mater.* 29 (2017) 5978–5982.
- [61] W.X. Zhang, J.C. Cui, C.A. Tao, Y.G. Wu, Z.P. Li, L. Ma, Y.Q. Wen, G.T. Li, *Angew. Chem. Int. Ed.* 121 (2009) 5978–5982.
- [62] J.H. Li, B. Shen, Z.H. Hong, B.Z. Lin, B.F. Gao, Y.L. Chen, *Chem. Commun.* 48 (2018) 12017–12019.
- [63] L.L. Xu, W. Li, J.L. Hu, X. Yang, F.Y. Ma, Y.N. Guo, X.D. Yu, Y.H. Guo, *J. Mater. Chem.* 19 (2009) 8571–8579.
- [64] P.C. Meng, H.M. Heng, Y.H. Sun, J.H. Huang, J.P. Yang, X. Liu, *Appl. Catal. B: Environ.* 226 (2018) 487–498.
- [65] Y. Wang, X.C. Wang, M. Antonietti, *Angew. Chem. Int. Ed.* 51 (2012) 68–69.
- [66] L. Li, Q.Y. Wu, Y.H. Guo, C.W. Hu, *Micropor. Mesoporous Mater.* 87 (2005) 1–5.
- [67] L.B. Jiang, X.Z. Yuan, G.M. Zeng, J. Liang, X.H. Chen, H.B. Yu, H. Wang, Z.B. Wu, J. Zhang, T. Xiong, *Appl. Catal. B: Environ.* 227 (2018) 376–385.
- [68] Z.Y. Fang, Y.Z. Hong, D. Li, B.F. Luo, B.D. Mao, W.D. Shi, *ACS Appl. Mater. Interfaces* 10 (2018) 20521–20529.
- [69] W.Y. Choi, J.Y. Ko, H. Park, J.S. Chung, *Appl. Catal. B: Environ.* 31 (2001) 209–220.
- [70] P.X. Qiu, C.M. Xu, H. Chen, F. Jiang, X. Wang, R.F. Lu, X.R. Zhang, *Appl. Catal. B: Environ.* 206 (2017) 319–327.
- [71] X.D. Du, Y.Q. Zhang, I. Hussain, S.B. Huang, W.L. Huang, *Chem. Eng. J.* 313 (2017) 1023–1032.
- [72] H.F. Shi, G. Yan, Y. Zhang, H.Q. Tan, W.Z. Zhou, Y.Y. Ma, Y.G. Li, W.L. Chen, E.B. Wang, *ACS Appl. Mater. Interfaces* 9 (2017) 422–430.
- [73] X.Y. Wang, J.Q. Meng, X. Yang, A. Hu, Y.X. Yang, Y.H. Guo, *ACS Appl. Mater. Interfaces* 11 (2019) 588–602.
- [74] Z. Wan, G.K. Zhang, X.Y. Wu, S. Yin, *Appl. Catal. B: Environ.* 207 (2017) 17–26.
- [75] P.Y. Liou, S.C. Chen, J.C.S. Wu, D. Liu, S. Mackintosh, M.M. Valer, R. Linforth, *Energy Environ. Sci.* 4 (2011) 1487–1494.